Ore Geology Reviews 86 (2017) 280–296

Contents lists available at ScienceDirect

Ore Geology Reviews

journal homepage: www.elsevier.com/locate/oregeo

Genesis of the Yandong porphyry Cu deposit in eastern Tianshan, NW China: Evidence from geology, fluid inclusions and isotope systematics

Yin-Hong Wang *, Fang-Fang Zhang, Bo-Chao Li

State Key Laboratory of Geological Processes and Mineral Resources, China University of Geosciences, Beijing 100083, China

ARTICLE INFO

Article history:
Received 17 December 2016
Received in revised form 16 February 2017
Accepted 21 February 2017
Available online 23 February 2017

Keywords:
Fluid inclusion
H–O–S isotopes
Yandong porphyry Cu deposit
Eastern Tianshan

ABSTRACT

The Yandong porphyry Cu deposit (372 Mt at 0.58% Cu) is located in the center of the eastern Tianshan, Xinjiang, NW China. Multiple-stage hydrothermal activities have resulted in potassic, chlorite-sericite, phyllic, and propylitic alteration in this deposit. The Yandong deposit formed in four stages, i.e., an early quartz ± magnetite ± pyrite stage (I), a quartz + pyrite ± chalcopyrite stage (II), a quartz + chalcopyrite ± pyrite ± molybdenite stage (III), and a late quartz + carbonate stage (IV). Three evolutionary episodes were observed by a detailed fluid inclusion study: (1) Early ore stage (I) fluids were trapped under two-phase conditions, as evidenced by the coexistence of vapor-rich (V-type) inclusions (homogenization temperatures = 410–494 °C, average salinity = 2.2 wt% NaCl equiv), liquid-rich (L-type) inclusions (homogenization temperatures = 311–430 °C, average salinity = 9.5 wt% NaCl equiv) and hypersaline (H-type) inclusions (trapped at ~300 bars, or a depth of approximately 1 km assuming lithostatic pressure conditions). (2) Main ore stage (II and III) fluid inclusions in quartz were also trapped under two-phase conditions (boiling), as identified by the coexistence of V- and L-type fluid inclusions; L-type inclusions homogenized between 161 and 390 °C (average = 270 °C), with salinities of 1.6–9.9 wt% NaCl equiv (average = 4.9 wt% NaCl equiv) and a depth of ~1 km (~100 bars, hydrostatic pressure conditions). (3) Late ore stage (IV) fluids are represented by inclusions in barren quartz–carbonate veinlets, characterized by homogenization temperatures ranging from 123 to 261 °C (average = 179 °C) and salinities between 0.7 and 4.7 wt% NaCl equiv (average = 2.0 wt% NaCl equiv). The initial hydrothermal fluids are characterized by high temperature, high salinity and high oxygen fugacity, belonging to a H_2O–NaCl system. Hydrogen and oxygen isotope data indicate that the hydrothermal fluids have a dominantly magmatic signature and mixed with abundant meteoric waters in the quartz-carbonate stage. Sulfur stable isotope suggests that the ore-forming metals came primarily from the tonalite magma that sourced from the subducted oceanic slab involving some mantle peridotites during ascent. The Cu mineralization of the Yandong porphyry deposit occurred at a shallow crustal level (approximately 1 km), and the fluid boiling or phase separation, decrease of temperature, as well as fluid-rock interaction were likely important factors responsible for metal accumulation and deposition in the magmatic-hydrothermal system.

1. Introduction

Being one of the largest accretionary orogens worldwide, the Central Asian Orogenic Belt (CAOB) extends for more than 5000 km from the Pacific Ocean to the European craton (Fig. 1a; Kovalenko et al., 2004; Zhang et al., 2009; Seltmann et al., 2014), and is bounded by the Tarim-North China craton to the south and by the Siberian craton to the north (Pirajno, 2010; Wilhem et al., 2012; Xiao et al., 2013, 2014; Li et al., 2015). The CAOB was produced as a consequence of multiple accretion and arc-continent collision events from the Early Neoproterozoic to the Late Paleozoic, driven by the successive closure of the paleo-Asian Ocean (Sengor et al., 1993; Windley et al., 2007; Xiao et al., 2010; Deng et al., 2014, 2015a; Deng and Wang, 2015). The southern CAOB in northwestern China consists, from north to the south, of the Chinese Altay, Junggar, Tianshan, and Beishan domains, which contains a number of Paleozoic hydrothermal ore deposits (Chen et al., 2010; Goldfarb et al., 2014; Deng et al., 2015b; Wang et al., 2015e; Porter, 2016; Zhang et al., 2016b). The most important porphyry deposits in northwestern China include Lamasu, Dabate, Lailisigaoer, Kendenggaoer, and Dongtujin in western Tianshan; Baogutu in Western Junggar; Xilekuduke,

* Corresponding author at: State Key Laboratory of Geological Processes and Mineral Resources, China University of Geosciences, 29 Xue-Yuan Road, Haidian District, Beijing 100083, China.
E-mail address: wyh@cugb.edu.cn (Y.-H. Wang).

http://dx.doi.org/10.1016/j.oregeorev.2017.02.020
0169-1368/

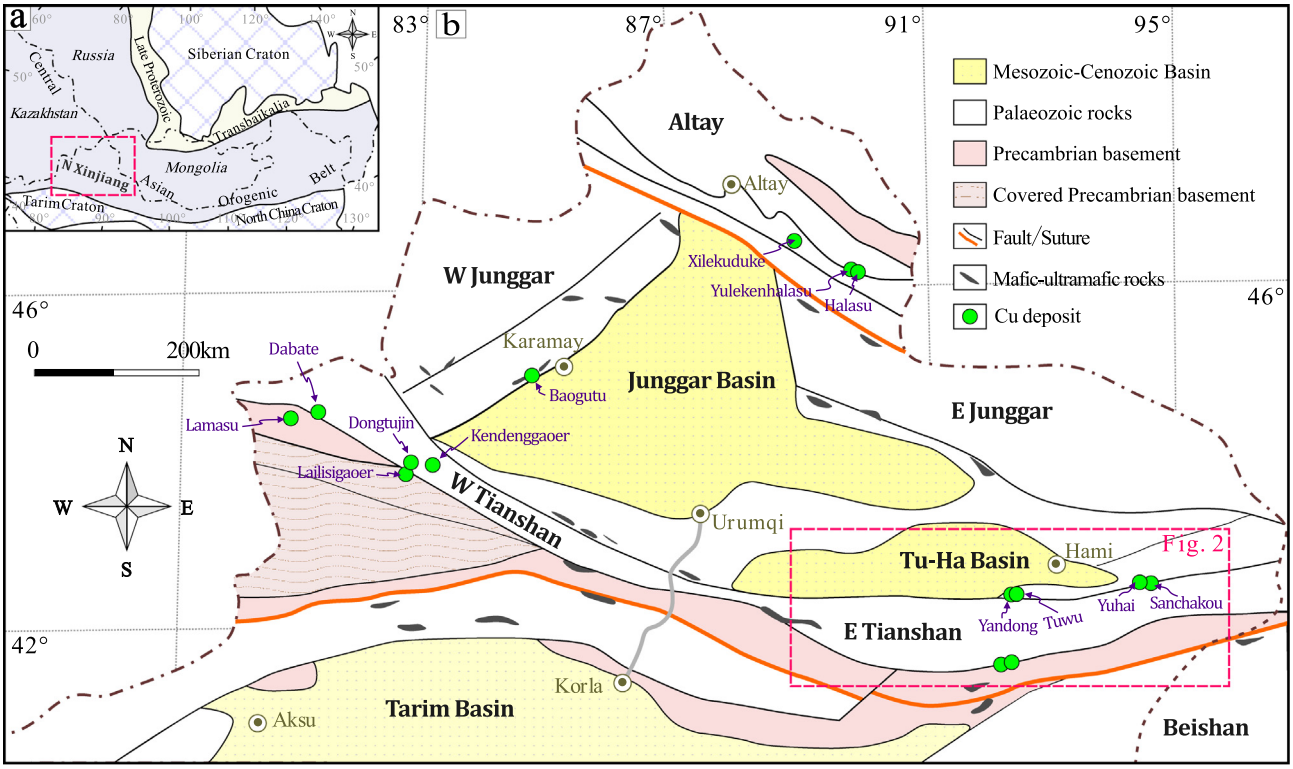

Fig. 1. (a) Location of the study area in the Central Asian Orogenic Belt (modified from Zhang et al., 2009); (b) Tectonic framework of the northwestern China showing major terranes, and locations of the Yandong porphyry Cu deposit and other major porphyry Cu deposits (modified from Chen et al., 2012b; Yang et al., 2012b; Zhu et al., 2012).

Yulekenhalasu and Halasu in Northern Junggar (Fig. 1b; Yang et al., 2010, 2014; Chen et al., 2012b; Shen et al., 2012, 2015). Most of these are porphyry Cu(–Mo) or Cu(–Au) deposits (Zhang et al., 2006b; Jia et al., 2011; Wan et al., 2015; Xue et al., 2016). The eastern Tianshan belt, situated within the southern part of the northwestern China, is also a significant Cu metallogenic belt (Fig. 1b; Qin et al., 2002; Zhai et al., 2011; Huang et al., 2013) and hosts many Cu deposits and occurrences (Fig. 2; Charvet et al., 2007; Singer et al., 2008; Pirajno et al., 2011; Chen et al., 2012b), including Yandong, Tuwu, Fuxing, Linglong, Chihu, Yuhai, and Sanchakou that are economically important and are primarily emplaced along the Dananhu-Tousuquan arc belt (Fig. 2; Rui et al., 2002; Zhang et al., 2008; Wang et al., 2016c,e; Wang and Zhang, 2016).

The Early Carboniferous Yandong deposit is one of the largest porphyry Cu deposits in the eastern Tianshan orogenic belt, Xinjiang, northwestern China (Figs. 1b and 2). It is located approximately 100 km southwest of Hami City, and was found in late 1990s by the No. 1 Geological Party, Xinjiang Bureau of Geology and Mineral Exploration. At present, it contains 2.1 Mt Cu from 372 Mt ores at an average grade of 0.58% Cu as well as significant amounts of Mo and Au (Singer et al., 2008; Seltmann et al., 2014). During the past two decades, the deposit has received much atten-

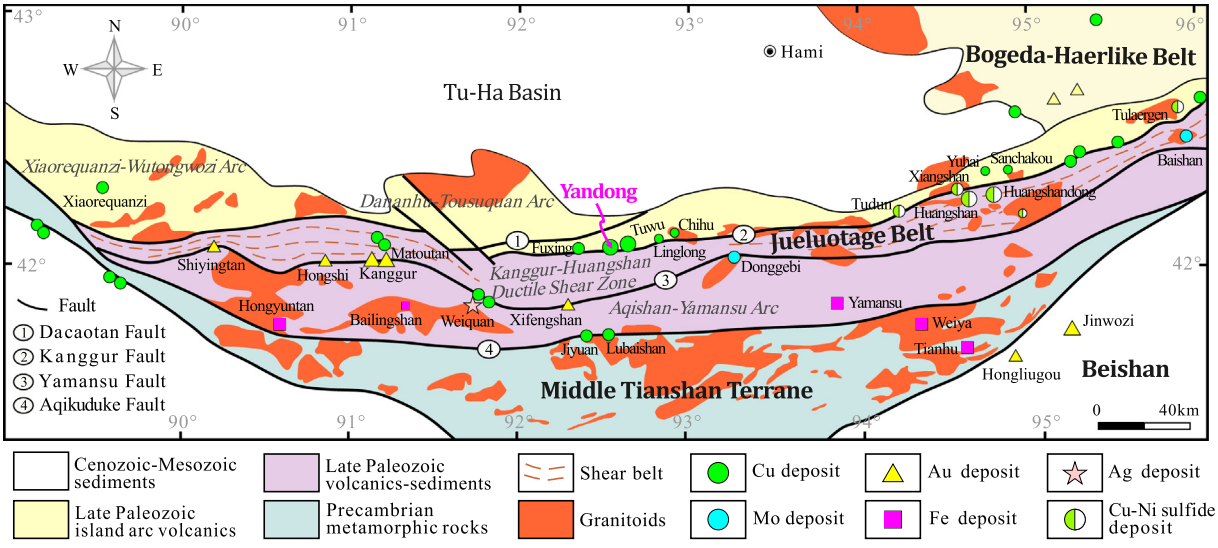

Fig. 2. Geological map of the eastern Tianshan showing major tectonic units, faults and metallic mineral deposits (modified from Huang et al., 2013).

tion that mainly focuses on the basic ore geology (Rui et al., 2002; Chen et al., 2005; Shen et al., 2014), geochronology (Zhang et al., 2006a; Shen et al., 2014), and petrogeochemistry (Hou et al., 2005; Wang et al., 2015b; Xiao et al., 2015). However, the evolution of the ore-forming fluids and source of the Yandong deposit are unknown but are crucial to determine the genesis of the deposit. In this paper, we reports new results obtained from ore geology research, fluid inclusion and stable isotope (H–O–S) studies for the Yandong deposit, in order to characterize and fingerprint the source of the hydrothermal fluids, as well as metallogenic process and ore genesis. Furthermore, the origin of the Yandong Cu deposit is discussed by integrating existing geological and geochronological data from other deposits in the eastern Tianshan region and other parts of the CAOB.

2. Regional geology

The eastern Tianshan orogenic belt, located between the Junggar Basin to the north and the Tarim Basin to the south (Fig. 1b; Chen et al., 2012b; Xiao et al., 2013; Goldfarb et al., 2014), can be divided into the Bogeda-Haerlike belt, the Jueluotage belt and the Middle Tianshan terrane from the north to the south (Fig. 2). The Bogeda-Haerlike belt comprises well-developed Ordovician-Carboniferous volcanic rocks, granites and mafic-ultramafic intrusions, and contains only few porphyry Cu and Au prospects (Fig. 2; Mao et al., 2005; Goldfarb et al., 2014; Gao et al., 2015). The Jueluotage Belt is characterized by Middle Paleozoic volcanic and sedimentary rocks, intruded by voluminous Carboniferous-Jurassic felsic and mafic-ultramafic complexes. The Middle Tianshan Terrane is comprised of Precambrian basement, and hosts some hydrothermal magnetite deposits (Seltmann et al., 2014; Shen et al., 2014). The Jueluotage belt can be subdivided into the Xiaorequanzi-Wutongwozi and Dananhu-Tousuquan arcs in the north, the Kanggur-Huangshan ductile shear zone in the central, and the Aqishan-Yamansu arc in the south, which are separated by the Kanggur and Yamansu faults (Fig. 2).

The Xiaorequanzi-Wutongwozi and Dananhu-Tousuquan arc belts are situated north of the Kanggur fault, and the strata exposed in the region include Lower Devonian volcanic and clastic sedimentary rocks of the Dananhu Formation, Lower Carboniferous turbidites of the Gandun Formation, Carboniferous basaltic to andesitic volcanic rocks and sedimentary rocks of the Qi'eshan Group, Permian calc-alkaline volcanic, pyroclastic and clastic rocks, Jurassic sandstone, and Cenozoic cover (Pirajno et al., 2011; Shen et al., 2014). In the Dananhu-Tousuquan arc, E-W trending faults including the Dacaotan and Kanggur faults, NW- and NE-trending strike-slip faults are present (Mao et al., 2005). The Kanggur-Huangshan ductile shear zone lies between the Kanggur and Yamansu faults, an area in which most rocks have undergone greenschist facies metamorphism and ductile deformation. The belt extends in a nearly E-W direction with a width of 10−30 km, and is well developed in eastern Tianshan (Fig. 2). It is characterized by a series of mylonites and mylonitized rocks. The typical metamorphic mineral assemblages are composed of actinolite, biotite and chlorite (Han et al., 2006; Zhang et al., 2008; Mao et al., 2015). There are a number of orogenic Au deposits (e.g., Kanggur and Hongshi), porphyry Mo deposits (e.g., Donggebi and Baishan), and magmatic Cu−Ni sulfide deposits (e.g., Huangshan and Huangshandong) that formed along the margin of the Kanggur-Huangshan ductile shear belt (Su et al., 2012; Wang et al., 2015c,d; Zhang et al., 2015, 2016c). The Aqishan-Yamansu arc belt, located between the Yamansu and Aqikuduke faults, is characterized by Early Carboniferous basalt, andesite, dacite, and tuff of the Yamansu Formation and Late Carboniferous rhyolite of the Tugutubulake Formation. Zircon LA-ICP-MS dating of the Yamansu basalt, Hongyuntan granodiorite, and Bailingshan granodiorite in the Aqishan-Yamansu arc belt yields age of 324.4 ± 0.94 Ma (Hou et al., 2014), 328.5 ± 9.3 Ma (Wu et al., 2006), and 317.7 ± 3.7 Ma (Zhou et al., 2010), respectively. The arc belt hosts numerous Fe (–Cu) (e.g., Yamansu and Hongyuntan) and Cu−Ag−Pb−Zn (e.g., Jiyuan) skarn deposits (Wu et al., 2006; Chen et al., 2012a; Hou et al., 2014).

The eastern Tianshan orogen has undergone a complex tectonic evolution from the Late Paleozoic to the Mesozoic, involving subduction of the paleo-Tianshan Ocean, collision-accretionary, strike-slip motion, post-collisional, and intracontinental extension (Xiao et al., 2004; Chen et al., 2011; Pirajno et al., 2011; Wang et al., 2016a,b). As a result, a series of E-W trending faults, together with extensive magmatism and mineralization were triggered during various stages. According to numerous studies, southward and northward subduction of the paleo-Tianshan oceanic plate could have been existing during the Early Carboniferous, triggering the formation of voluminous intrusive rock emplacement in the region (Mao et al., 2005; Zhang et al., 2008; Gao et al., 2015; Wang et al., 2016d,e). These intrusions consists of syenogranite, granodiorite, tonalite, and diorite porphyry, and are spatially and genetically related to a number of porphyry Cu deposits distributed in the Dananhu-Tousuquan arc (e.g., Yandong, Tuwu, Linglong, Chihu, Fuxing, and Yuhai). Following elimination of the paleo-Tianshan Ocean, arc-continent and continent-continent collision occurred in the Late Carboniferous, associated with inductile deformation and thrusting (Zhang et al., 2008). At the same time, the Kanggur-Huangshan ductile shear zone was formed, and syn-tectonic magmatism and metamorphism resulted in extensive alteration of the Carboniferous volcanic rocks (Huang et al., 2013). The eastern Tianshan entered into a post-collisional setting since the Early Permian (Qin et al., 2002; Su et al., 2012; Huang et al., 2013), evidenced by the emplacement of mafic-ultramafic and granitic intrusions with ages from 300 to 270 Ma. However, the Mesozoic tectonic evolution of eastern Tianshan is characterized by intracontinental extension, with ages constrained by the within-plate igneous rocks (~250–230 Ma; Han et al., 2006; Zhang et al., 2015).

3. Geology of the deposit

The Yandong porphyry Cu deposit is located in the southern part of the Dananhu–Tousuquan arc belt, eastern Tianshan, close to the E-W trending Kanggur fault (Fig. 2). A series of EW-trending ductile shear faults that are the secondary faults of the Kanggur-Huangshan ductile shear zone developed in the deposit (Fig. 3a, b), whereas NW-trending structures are also present within the area. Ore bodies are mainly hosted in the diorite, tonalite, and quartz porphyries that intruded intermediate to mafic volcanic rocks of the Qi'eshan Group (Zhang et al., 2006a; Shen et al., 2014; Wang et al., 2015b; Fig. 4). The Qi'eshan Group is divided into three lithologic units (Han et al., 2006; Wang et al., 2015b). Unit 1 consists of andesite and basalt intercalated with tuff. Unit 2 consists of andesite and brecciated andesite. Unit 3 consists of pebbly lithic sandstone and minor tuffaceous sediments intercalated with basalt, andesite and dacite flows. The strata of the Qi'eshan Group are 600–2000 m thick, stretching in an ENE-WSE direction and dipping to the south at angles of 43–63° (Shen et al., 2014). The overlying rocks of the Jurassic Xishanyao Formation consist chiefly of sandstone, siltite, mudstone and conglomerate, and form an angular unconformity with the strata of the Qi'eshan Group (Fig. 3b). The units are covered by a thin layer of Jurassic strata (Fig. 4).

The Carboniferous porphyry intrusions predominantly include diorite porphyry, tonalite (also named plagiogranite porphyry in

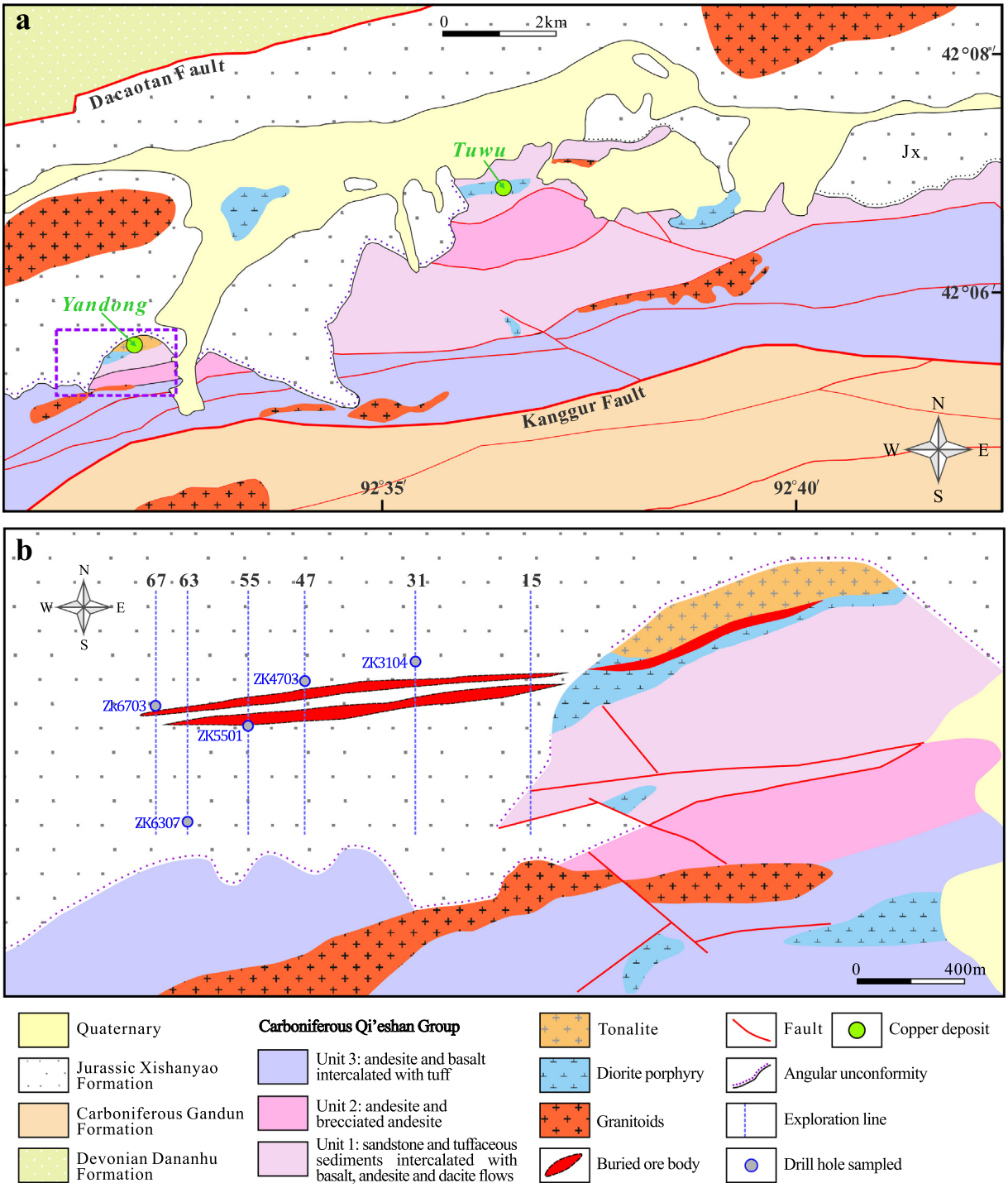

Fig. 3. (a) Geological map of the Tuwu–Yandong porphyry Cu belt in eastern Tianshan (modified from Zhang et al., 2010a); (b) Geological map of the Yandong porphyry Cu deposit (modified from Zhang et al., 2010a).

some literature), and quartz porphyry. Among them, the tonalite intrusions are considered to be related the porphyry-style Cu mineralization at Yandong. They generally occurred as dykes and intruded the diorite porphyry and the Qi'eshan Group rocks (Fig. 4). It is light grey or greyish white colored, and is characterized by a medium- or fine-grained weak gneissic texture, massive structure and intensive alteration (e.g. potassic alteration and sericitization). It typically contains plagioclase (35–45%), quartz (30–40%) and biotite (5–10%), with accessory minerals of zircon, apatite, and magnetite. Our previous studies (data below from Wang et al., 2015b) reveal that the tonalite was emplaced at 335.0 ± 3.7 Ma (MSWD = 0.97) by SHRIMP zircon U–Pb dating. They have a geochemical affinity with modern adakites, which are characterized by high SiO_2 contents, no or positive Eu anomalies, high La/Yb ratios and Sr contents, low Y and HREE contents, positive K, Rb, Sr, and Ba but negative Nb, Ta, P, and Ti anomalies. The adakitic tonalite intrusions display high $Mg^{\#}$ values, positive zircon $\varepsilon_{Hf}(t)$ values (+9.4 to +15.8), and young Hf model ages

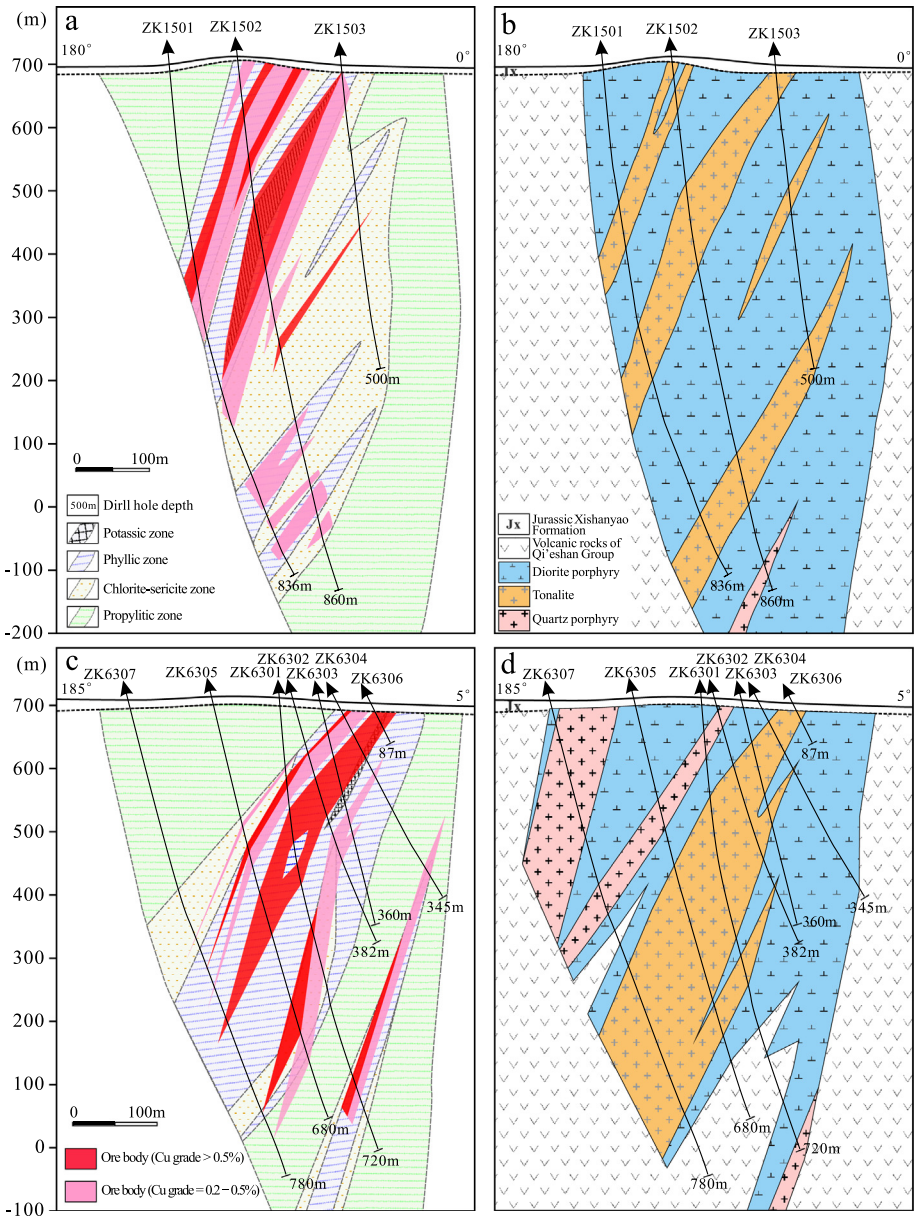

Fig. 4. Geological cross section along section Line 15 and 63 with orebody (a, c) and lithologies (b, d) in the Yandong porphyry Cu deposit (modified from Shen et al., 2014).

(334–750 Ma), indicating that their parental magma was most likely derived from partial melting of the subducted oceanic crust hybridized by peridotite in the mantle wedge (Wang et al., 2015b)

The Yandong orebody has a tabular morphology and is elongated in the E–W direction. It is generally covered by Jurassic Xishanyao Formation sandstone and poorly exposed (Fig. 3b). The main orebody is about 1400 m in length and 33 m in thickness, and dips steeply to the south at angles of 68–88° (Zhang et al., 2006a; Wang et al., 2015b). There is no distinct boundary between the orebodies and country rocks. The mineralized bodies have an elongated shape with their long axes parallel to the tonalite dykes dykes in the dip direction. Mineralization is better developed in the northern parts of the Yandong area, and the highest grade (>0.5% Cu) zones occur at depths of ~100 to 500 m depth below the surface, associated with intensive phyllic and chlorite alteration assemblages. In addition, significant amounts of Au and Mo mineralization have been detected at depth in the porphyry hosts (Rui et al., 2002; Mao et al., 2005; Zhang et al., 2006a). Sulfide mineralization in the Yandong deposit occurs as veinlets or disseminations. Gangue minerals are composed of quartz, sericite, and chlorite with minor biotite, amphibole, epidote, anhydrite, and calcite (Fig. 5a-f). Ore minerals are dominated by chalcopyrite and pyrite with minor molybdenite, bornite, and chalcocite (Fig. 5g-i).

Rocks within the Yandong deposit record intense hydrothermal alteration, especially within and adjacent to the porphyry intrusions. The alteration associated with Cu mineralization in the Yandong deposit includes potassic, propylitic, chlorite–sericite and phyllic alteration (Fig. 4). The alteration zones of the mineralized porphyry bodies are similar to those of other porphyry Cu deposits in the eastern Tianshan orogenic belt (Zhang et al., 2006a; Shen et al., 2014; Gao et al., 2015). The mineralization processes in the Yandong porphyry Cu deposit are divided into four stages from early to late (Fig. 6), based on mineral assemblages and fabrics as well as on crosscutting relationships. Stage I quartz ± magnetite ± pyrite veins are characterized by quartz and minor disseminated mineralization associated with local potassic alteration in hosting rocks (Fig. 7a). Stage II is represented by widespread quartz + pyrite ± chalcopyrite veins or veinlets (Fig. 7b, c, d) and

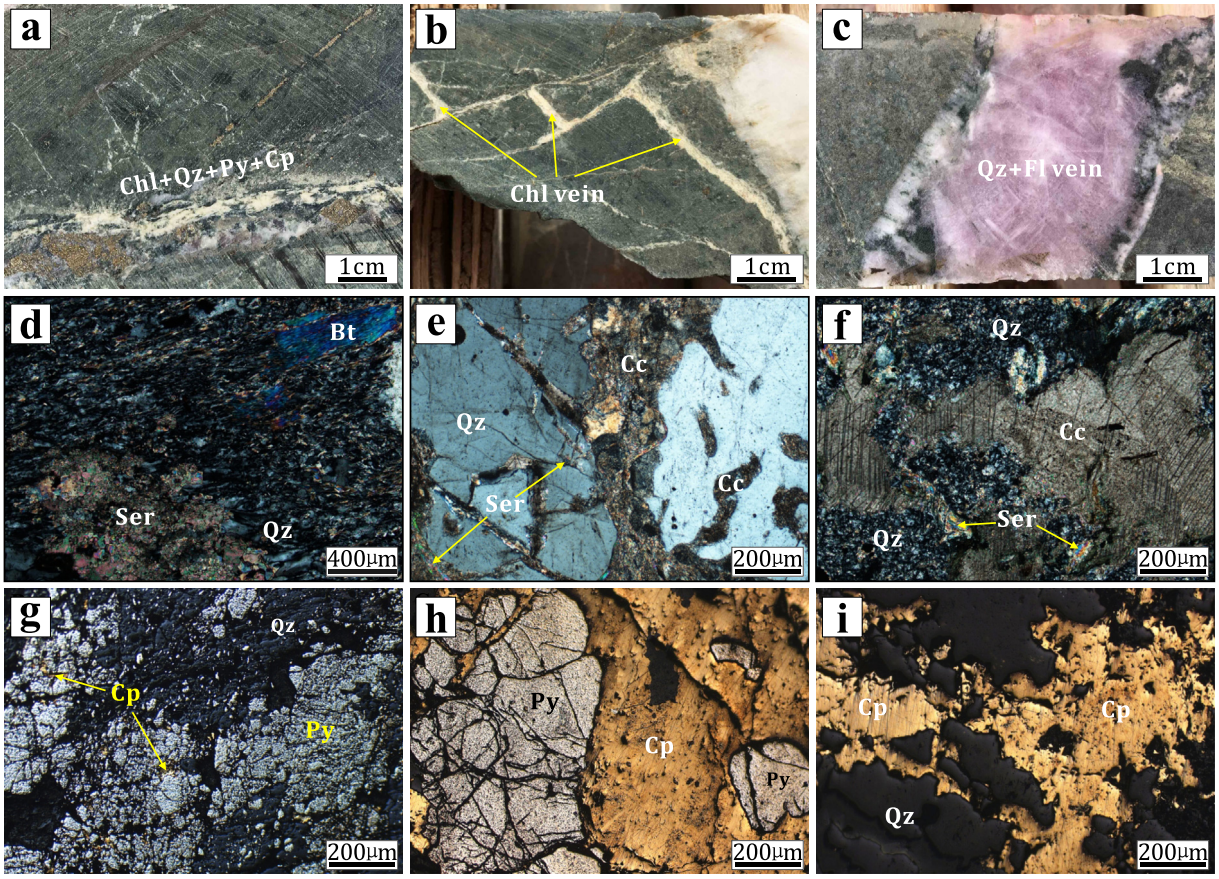

Fig. 5. Photographs and photomicrographs of hydrothermal alteration (a–f) and mineralization (g–i) features in the Yandong porphyry Cu deposit. (a) Chloritization and associated chlorite – quartz – pyrite – chalcopyrite vein in diorite porphyry; (b) Chlorite vein cut by late quartz – calcite vein in diorite porphyry; (c) Quatz – fluorite alteration assemblages in diorite porphyry; (d) secondary biotite locally overprinted by sericite in tonalite; (e, f) Calcite as a late phase locally overprinting early sericitization in tonalite; (g) Anhedral pyrite and minor chalcopyrite in diorite porphyry; (h) Chalcopyrite – pyrite vein in tonalite; (i) Disseminated chalcopyrite – quartz vein in tonalite. Mineral abbreviations: Qz = quartz, Bt = biotite, Py = pyrite, Cp = chalcopyrite, Ser = sericite, Chl = chlorite, Cc = calcite, Fl = fluorite.

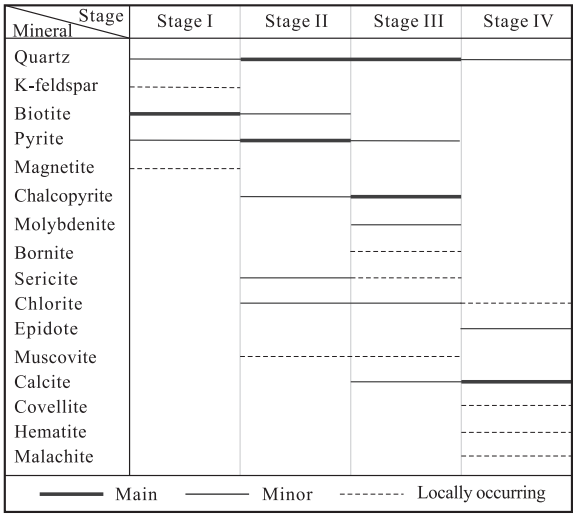

Fig. 6. Paragenetic sequence for the Yandong porphyry Cu deposit.

minor disseminated mineralization associated with extensive chlorite-sericite alteration (Fig. 5a). Stage III has mineral assemblages of quartz + chalcopyrite + pyrite (Fig. 7d), quartz + chalcopyrite (Fig. 7e), quartz + chalcopyrite + bornite (Fig. 7f, g), and quartz + molybdenite ± pyrite ± chalcopyrite (Fig. 7h, i) occurring as veins or veinlets. Coeval alteration includes phyllic alteration and chloritization. The stages II and III are the main Cu mineralization stage, and large amounts of chalcopyrite were precipitated during the stages, associated with other sulfide minerals (e.g., pyrite, molybdenite, and bornite). They are typically thick, chalcopyrite rich (±pyrite) or molybdenite rich (±chalcopyrite ± pyrite), and have cut stage II quartz + pyrite veins (Fig. 7d). Stage IV is defined by barren veinlets of quartz + carbonate, which generally cut the earlier-formed veins or veinlets (Fig. 7j).

4. Sampling and analytical methods

4.1. Fluid inclusion analyses

Fluid inclusion study was conducted on fifteen samples collected from mineralized quartz veins of different stages. The samples consist of quartz and variable amounts of pyrite and chalcopyrite, with or without molybdenite. Polished thin sections were examined under microscope to identify the phase, shape, size, distribution, and thus possible origin of the fluid inclusions. Microthermometric measurements and Laser Raman spectroscopic analyses were carried out at Resources Exploration Laboratory, China University of Geosciences, Beijing. Fluid inclusion microthermometry data were obtained using a Linkam MDS 600 heating-freezing stage equipped with a Zeiss microscope. The measurements consist of ice-melting temperature ($T_{m,\ ice}$), halite dissolution temperature ($T_{s,\ halite}$), and homogenization temperature (T_h). Laser Raman spectroscopic analyses of selected fluid inclu-

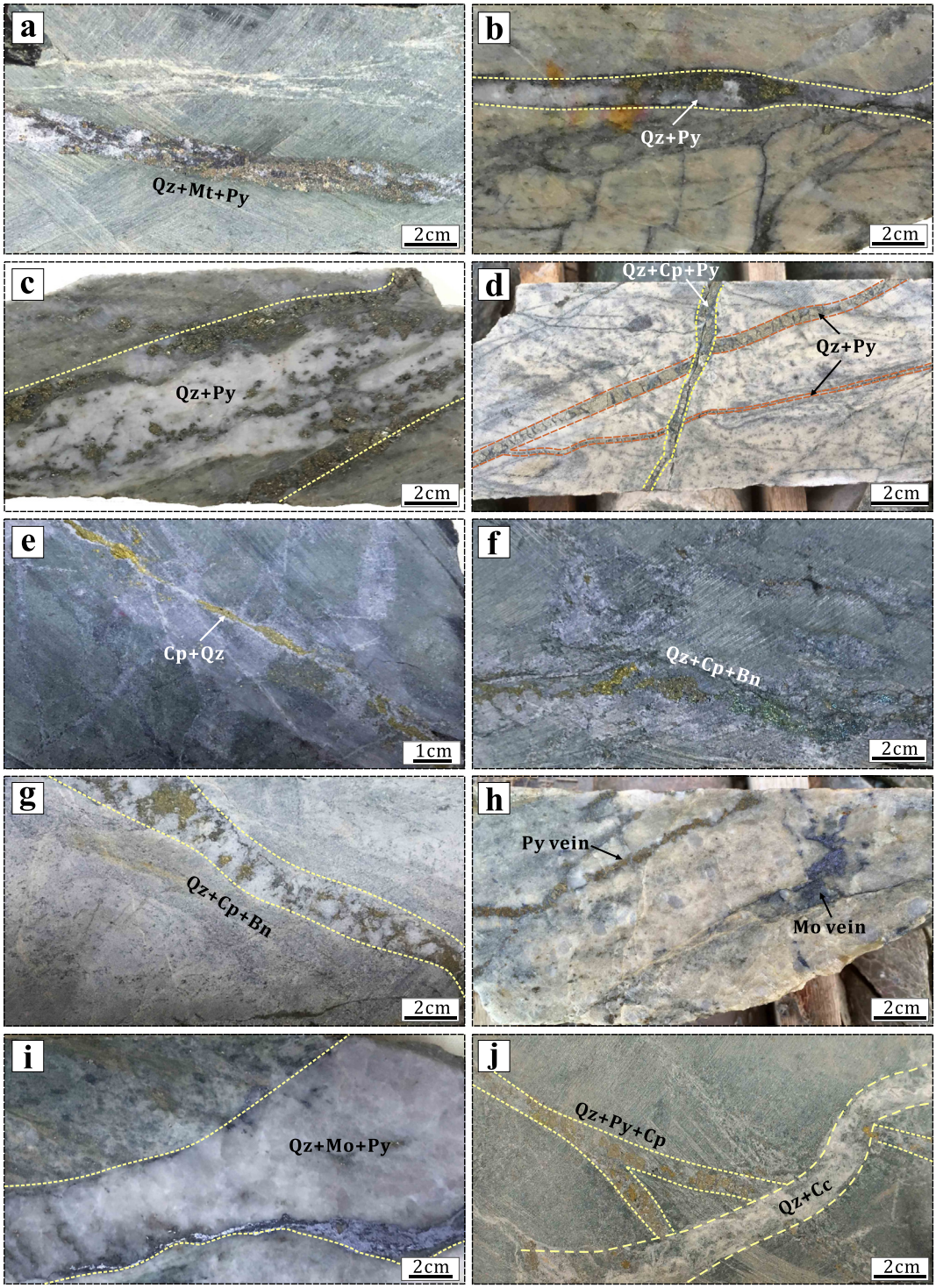

Fig. 7. Photographs showing ore fabrics and mineral assemblages of the Yandong porphyry Cu deposit. (a) quartz – magnetite – pyrite vein of stage I in diorite porphyry; (b, c) Fine-grained quartz – pyrite vein of stage II in tonalite; (d) quartz – pyrite – chalcopyrite vein of stage III cutting earlier quartz – pyrite vein in tonalite; (e) quartz – chalcopyrite of stage III in diorite porphyry; (f) quartz – chalcopyrite – bornite vein of stage III in diorite porphyry; (g) quartz – chalcopyrite – bornite vein of stage III in tonalite; (h) early quartz – pyrite vein and disseminated molybdenite of stage III in tonalite with chlorite – sericite alteration; (i) quartz – molybdenite – pyrite of stage III in tonalite; (j) quartz – calcite vein of stage IV cutting quartz – pyrite – chalcopyrite vein of stage III in diorite porphyry. Mineral abbreviations: Qz = quartz, Py = pyrite, Mt = magnetite, Cp = chalcopyrite, Bn = bornite, Mo = molybdenite, Cc = calcite.

sions were carried out with a Renishaw inVia Raman scanning spectrometer, operating with an excitation wave length of λ = 514.5 nm. The equation of Bodnar (1993) was used to calculate salinities of the aqueous two-phase fluid inclusions from measured final ice-melting temperatures. Salinities of hypersaline inclusions were calculated from measured halite-melting temperatures using the equation of Lecumberri-Sanchez et al. (2012).

4.2. H–O isotope analyses

Ten quartz samples were collected from various types of quartz–sulfide veins and quartz–calcite veins for hydrogen and oxygen isotope analyses, which were accomplished using a MAT 253EM mass spectrometer, at the Institute of Mineral Resources, Chinese Academy of Geological Sciences, Beijing. Oxygen was liber-

ated from quartz by reaction with BrF_5, and converted to CO_2 on a platinum-coated carbon rod for oxygen isotope analysis (Clayton and Mayeda, 1963). δD values were measured on water in fluid inclusions decrepitated from quartz and the water was released by heating the quartz to above 500 °C by means of an induction furnace, and then reacted with chromium powder at 800 °C to obtain hydrogen for isotopic analysis. The isotopic data are reported relative to the Standard Mean Ocean Water (SMOW) standard for $\delta^{18}O$ and δD, and the analytic precision is ±0.2‰ for $\delta^{18}O$, and ±2‰ for δD values.

4.3. S isotope analyses

Nine pyrite and two chalcopyrite samples from different mineralization stages (I, II, and III) were chosen for sulfur isotope analyses. Sulfur isotopie compositions were conducted using a Finnigan MAT 251EM mass spectrometer, at the Analytical Laboratory of the Beijing Research Institute of Uranium Geology. The $\delta^{34}S$ of sulfide was determined on SO_2 obtained by placing the sulfide-CuO composite (at weight ratio of 1/7) into a vacuum system heated to 980 °C. Sulfur isotope ratios are expressed as per mil deviations from the sulfur isotope composition of the Cañon Diablo Troilite (CDT) using the conventional delta ($\delta^{34}S$) notation. Sulfur isotope results are generally reproducible within ± 0.2‰ (2σ) in the laboratory.

5. Fluid inclusion results

5.1. Petrography and types of fluid inclusions

All samples contain abundant primary and secondary inclusions (Roedder, 1984), with irregular, ovoid, and negative crystal forms. Based on the textural criteria of Roedder (1984), only primary inclusions were analyzed in this study. Secondary inclusions were not used, which generally occur in annealed trails penetrating crystal boundary. Three types of primary inclusions have been distinguished, based on textural, paragenetic, and phase proportion at room temperature. They are type 1: two-phase liquid-rich inclusions; type 2: mono-phase vapor or two-phase vapor-rich inclusions; type 3: three-phase hypersaline inclusions with halite and other daughter crystals (Fig. 8).

Liquid-rich (L-type) inclusions are the most common type in stage I to stage IV quartz veins. They consist of a liquid phase (L_{H2O}) and a vapor bubble (V_{H2O}) with the liquid phase volumetrically dominant, and vary from native-crystal to highly irregular shape (Fig. 8a, b, f–g). This type inclusion mainly homogenized to liquid, rarely to vapor. They are smaller in size from 3 to 13 μm, and have a vapor volume varying from 10 to 30 percent. Generally, L-type inclusions occur throughout both the massive and disseminated ores.

Vapor-rich (V-type) inclusions are detected in stage I to stage III quartz veins, and consist of vapor and liquid phases with the vapor phase volumetrically dominant. They mostly occur as irregular isolations, and individual fluid inclusions are distributed randomly, commonly coexisting with the L-type inclusions (Fig. 8e, m). This type inclusion mainly homogenized to vapor, rarely to critical behavior. These inclusions range in diameter from 3 to 11 μm, in which vapor bubbles account 50–80 percent of total volume (Fig. 8i, j). Some mono-phase vapor inclusions are also detected in stage I quartz vein, and usually have native-crystal shapes (Fig. 8c).

Hypersaline (H-type) inclusions are mainly present in quartz from stage I (Fig. 8d) and commonly occur with vapor-rich inclusions (H + V assemblages), indicating immiscibility features. They consist of liquid + vapor + halite ± other daughter crystals, and generally occur in negative crystal shapes and vary from 4 to 9 μm in size. This type inclusion homogenized by halite dissolution after bubble disappearance, and is rarely detected in quartz veins at Yandong.

5.2. Microthermometric results

The microthermometric data and calculated parameters for fluid inclusions are summarized in Table 1 and graphically illustrated in Figs. 9 and 10. Raman spectra of selected fluid inclusions are shown in Fig. 11. As noted above, the L + V inclusions are widespread in stage II and III quartz veins (intergrown with chalcopyrite and pyrite), whereas the H inclusions are recognized in stage I quartz veins. Late ore stage quartz-carbonate veinlets contain only L-type fluid inclusions.

Stage I quartz: All the L-type inclusions homogenized to the aqueous liquid phase during heating, with homogenization temperatures ranging from 311 to 430 °C (average = 381 °C, n = 14; Fig. 9a). Final melting temperatures of ice are between −9.5 and −5.0 °C, corresponding to salinities of 7.9–13.4 wt% NaCl equiv (Bodnar, 1993), with a mean of 9.5 wt% NaCl equiv Densities of these fluid inclusions are estimated to be 0.71–0.86 g/cm^3 (Table 1), using the program of Mao and Duan (2008).

V-type inclusions were present with L-type inclusions in some quartz veins (Fig. 8b). Most V-type inclusions homogenized into the vapor phase, and a few homogenized into aqueous liquid phase. The homogenization temperatures range from 410 to 494 °C (average = 457 °C, n = 11; Fig. 9a). Final melting temperatures of ice are between −1.9 to −0.8 °C, corresponding to salinities of 1.4–3.2 wt% NaCl equiv (Bodnar, 1993), with a mean of 2.2 wt% NaCl equiv The densities of these fluid inclusions are relatively lower, ranging from 0.30 to 0.39 g/cm^3 (Table 1).

For H-type inclusions, they commonly occur together with V-type inclusions (Fig. 8d), indicating immiscibility features. All the H-type inclusions homogenized to the liquid phase with daughter minerals dissolving before bubble disappearance, with a range of final homogenization temperatures from 425 to 521 °C (average = 475 °C, n = 10; Fig. 9a). Salinity calculated from these fluid inclusions range from 49.8 to 62.6 wt% NaCl equiv (Sterner et al., 1988; Fig. 10), with a mean of 56.5 wt% NaCl equiv The densities of these fluid inclusions are relatively higher, ranging from 1.87 to 2.12 g/cm^3 (Table 1).

Stage II quartz: All the L-type inclusions homogenized to the aqueous liquid phase during heating, with homogenization temperatures ranging from 225 to 390 °C (average = 290 °C, n = 41; Fig. 9c). Final melting temperatures of ice are between −6.5 and −1.4 °C, corresponding to salinities of 2.4–9.9 wt% NaCl equiv (Bodnar, 1993), with a mean of 5.3 wt% NaCl equiv Densities of these fluid inclusions are estimated to be 0.56–0.89 g/cm^3 (Table 1).

V-type inclusions were present with L-type inclusions in some quartz veins (Fig. 8e), implying that the system formed close to or on the two-phase line. Most V-type inclusions homogenized into the vapor phase, and a few homogenized into aqueous liquid phase. The homogenization temperatures range from 279 to 367 °C (average = 309 °C, n = 10; Fig. 10). Final melting temperatures of ice are between −2.1 to −0.6 °C, corresponding to salinities of 1.1–3.6 wt% NaCl equiv (Bodnar, 1993), with a mean of 1.9 wt% NaCl equiv.

Stage III quartz: L-type inclusions are the most abundant type in the ore stage III quartz veins, and all homogenized into the aqueous liquid phase at between 161 and 348 °C (average = 251 °C, n = 55; Fig. 9e). Final melting temperatures of ice range from −4.8 to −0.9 °C, corresponding to salinities of 1.6–7.6 wt% NaCl equiv (Bodnar, 1993), with a mean of 4.4 wt% NaCl equiv The den-

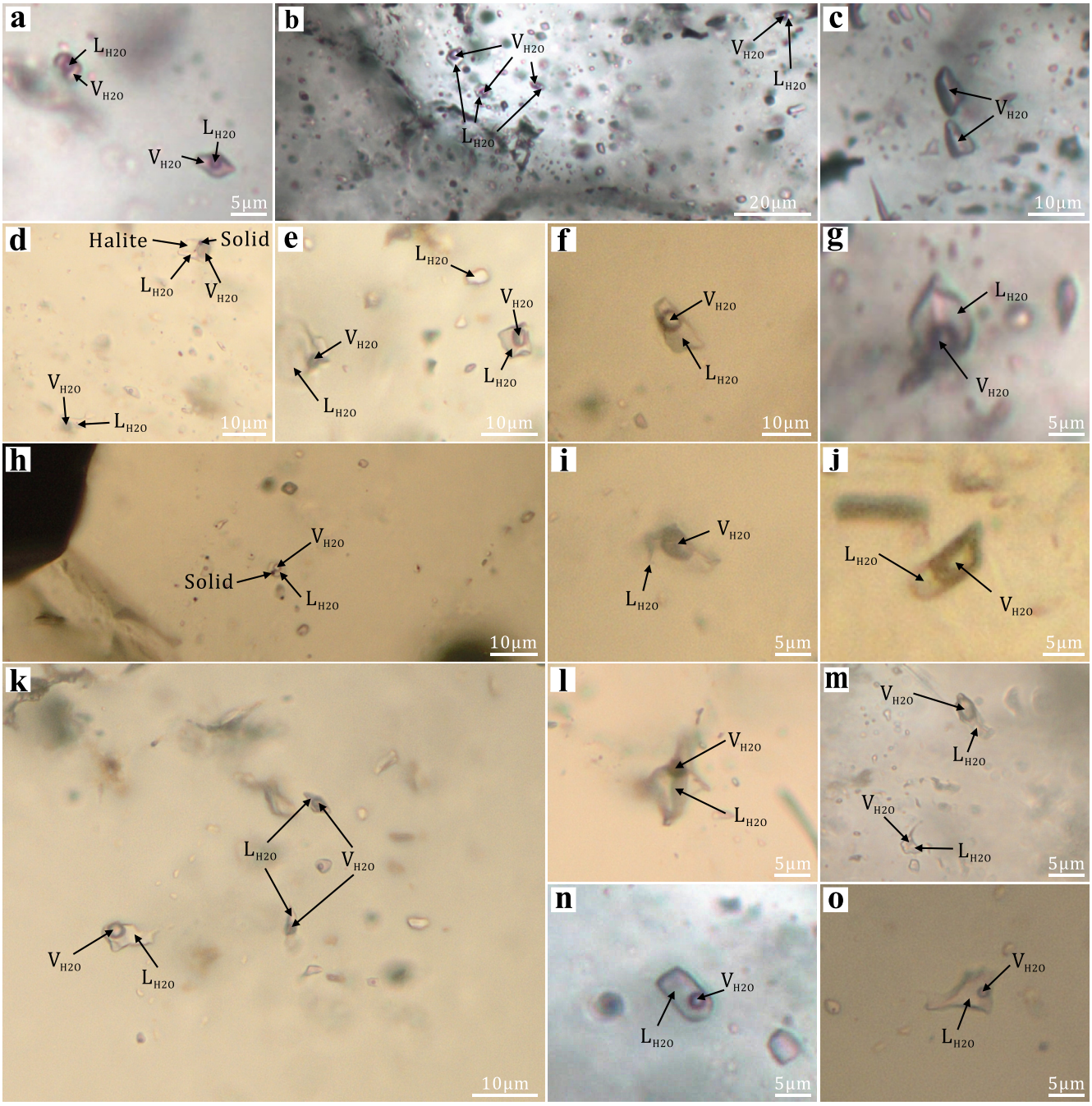

Fig. 8. Photomicrographs showing the types and distribution of fluid inclusions trapped in mineralized quartz. (a) Ovoid liquid-rich two-phase aqueous inclusions from stage I quartz; (b) Cluster of liquid-rich two-phase aqueous inclusions associated with vapor-rich inclusions, from stage I quartz; (c) Isolations of mono-phase vapor inclusions with negative crystal forms from stage I quartz; (d) Hypersaline inclusion from stage I quartz, coexisting with vapor-rich inclusion; (e) Coexisting two-phase aqueous inclusions and mono-phase liquid inclusion from stage II quartz; (f, g) Isolation of liquid-rich two-phase aqueous inclusion from stage II quartz; (h) Multi-phase inclusion containing an opaque solid from stage III quartz; (i, j) Vapor-rich two-phase aqueous inclusions from stage III quartz; (k, l) Liquid-rich two-phase aqueous inclusions from stage III quartz; (m) Coexisting vapor-rich and liquid-rich two-phase aqueous inclusions from stage III quartz; (n) Ovoid liquid-rich two-phase aqueous inclusion from stage IV quartz; (o) Irregular liquid-rich two-phase aqueous inclusion from stage IV quartz.

sities of these fluid inclusions are estimated to be 0.76–0.98 g/cm^3 (Table 1).

V-type inclusions are relatively rare than L-type inclusions in the ore stage III quartz veins, and all V-type inclusions also homogenized into the aqueous liquid phase. The homogenization temperatures range from 253 to 321 °C (average = 287 °C, n = 6; Fig. 9e). Final melting temperatures of ice are between −1.1 and −0.4 °C, corresponding to salinities of 0.7–1.9 wt% NaCl equiv (Bodnar, 1993). The coexistence of V-type and L-type fluid inclusions (Fig. 8m) indicates that the system formed close to or on the two-phase line. We thus suggest that boiling continued during the ore stage III.

Stage IV quartz: L-type inclusions are the only type recognized in the stage IV quartz veins (Fig. 8n, o), and all homogenized into the aqueous liquid phase at between 123 and 261 °C (average = 179 °C, n = 18; Fig. 9g). Final melting temperatures of ice vary from −2.8 to −0.4 °C, equivalent to salinities of 0.7–4.7 wt% NaCl equiv (Bodnar, 1993), with a mean of 2.0 wt% NaCl equiv The densities of these

Table 1
Summary of microthermometric data and calculated parameters for fluid inclusions in the Yandong mineralized quartz.

Stage	Samples	FI type[1]	Size (μm)	$T_{m,ice}$ (°C)	T_h (°C)	$T_{s,halite}$ (°C)	Salinity (wt% NaCl equiv)[2]	Bulk density (g/cm^3)
Stage I	Quartz ± magnetite ± pyrite	L	4–10	−9.5 to −5.0	311–430		7.9–13.4	0.71–0.86
		V	3–8	−1.9 to −0.8	410–494		1.4–3.2	0.30–0.39
		H	4–9		325–410	425–521	49.8–62.6	1.87–2.12
Stage II	Quartz + pyrite ± chalcopyrite vein	L	4–12	−6.5 to −1.4	225–390		2.4–9.9	0.56–0.89
		V	3–11	−2.1 to −0.6	279–367		1.1–3.6	0.56–0.77
Stage III	Quartz + chalcopyrite ± pyrite ± molybdenite vein	L	3–13	−4.8 to −0.9	161–348		1.6–7.6	0.76–0.98
		V	5–10	−1.1 to −0.4	253–321		0.7–1.9	0.71–0.82
Stage IV	Quartz + carbonate vein	L	3–9	−2.8 to −0.4	123–261		0.7–4.7	0.83–0.98

[1] Fluid inclusion type: L = liquid-rich; V = vapor-rich; H = hypersline.
[2] Methods used for calculating the salinity and density of the fluid inclusions are described in the text.

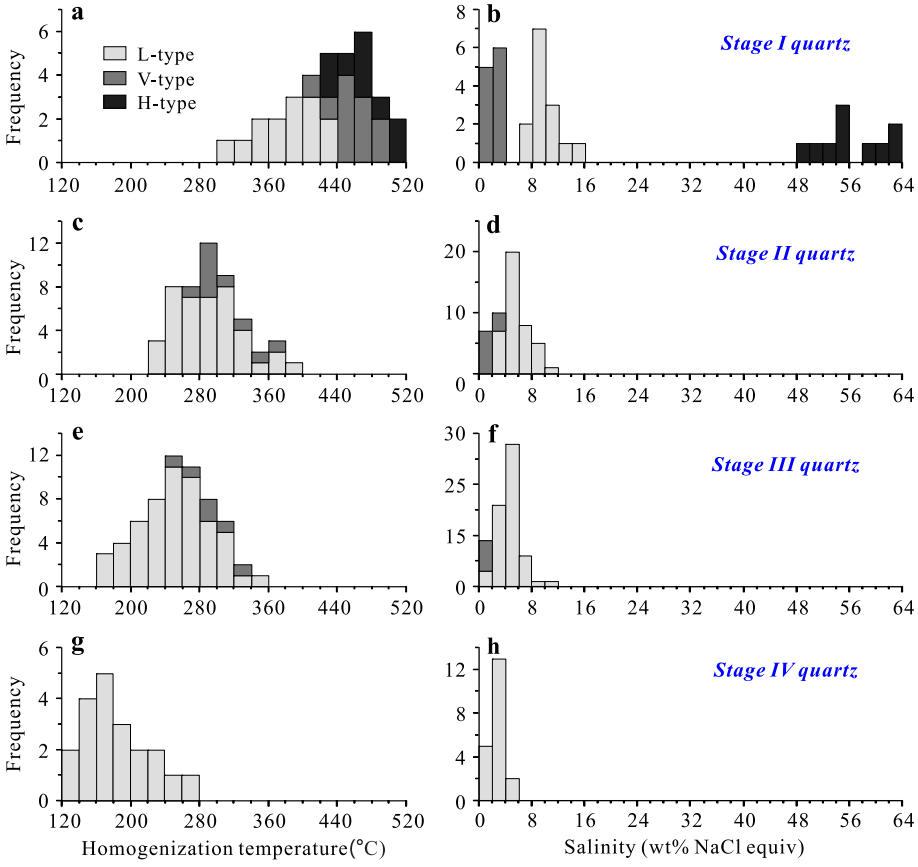

Fig. 9. Histograms of homogenization temperature and salinity for all inclusion types in different stages quartz.

fluid inclusions are estimated to be 0.83–0.98 g/cm^3 (Table 1). Clear evidence of boiling was absent in this ore stage.

5.3. Pressure estimation and mineralization depth

Estimates of trapping pressure can be conducted only when the actual trapping temperature is known, or if fluid boiling or immiscibility occurred in the system at the time of entrapment (Roedder and Bodnar, 1980). As described above, evidence of immiscibility was observed in the quartz ± magnetite ± pyrite vein of the stage I, and fluid boiling was observed in quartz + pyrite ± chalcopyrite vein of the stage II, and quartz + chalcopyrite ± pyrite ± molybdenite vein of the stage III, corresponding to peak homogenization temperature intervals of 420–480 °C, 280–320 °C, and 240–280 °C, respectively. Thus, homogenization temperatures are interpreted to closely approximate trapping temperatures. Trapping pressures can be estimated based on the homogenization temperatures and salinities of the fluid inclusions (L, V and H-types) in quartz-sulfide vein, using the isobar equations from Driesner and Heinrich (2007). However, the lack of evidence for fluid boiling in the stage IV only permits the estimation of minimum trapping temperatures and pressures for the late ore-forming fluids (Zhu et al., 2015). As shown in Fig. 12, the trapping pressures for H-type fluid inclusions of the early ore stage (I) are estimated ranging from 200 to 400 bars, with an average of ~300 bars. For the coexisting V- and L-type inclusions of the main ore stage (II and III), the estimated trapping pressures are concentrated at ~100 bars. These pressures are equivalent to a trapping depth of ~1 km if lithostatic pressures are assumed in the

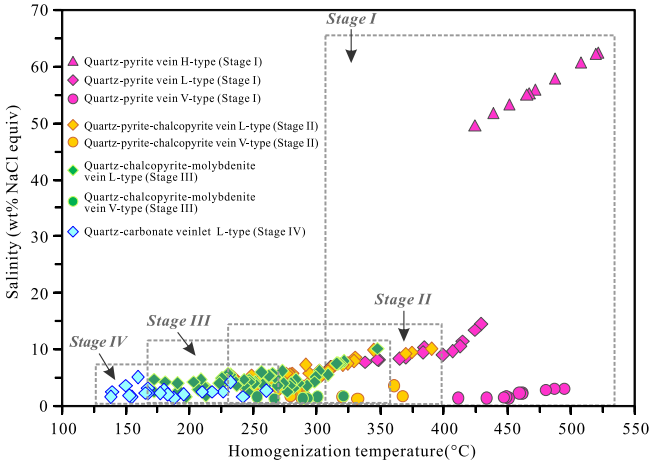

Fig. 10. Summary plot of homogenization temperatures and salinities of individual fluid inclusions of different stages for the Yandong porphyry Cu deposit.

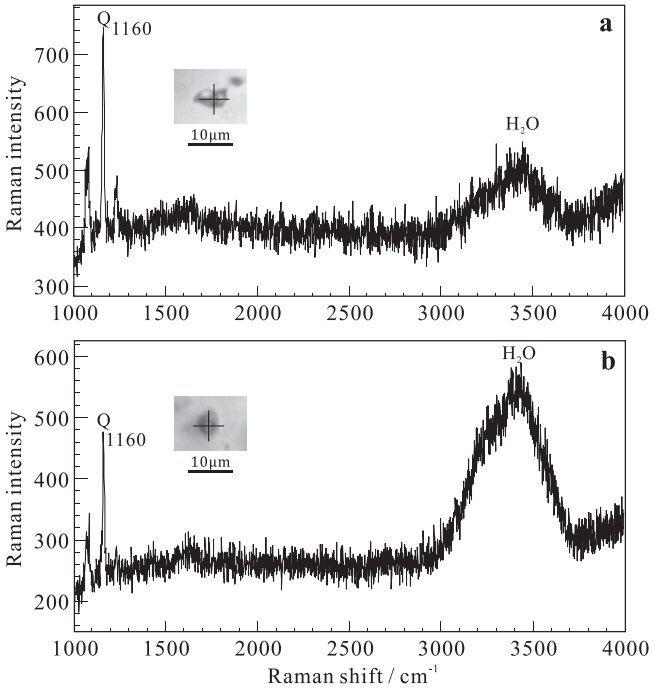

Fig. 11. Laser Raman spectra for aqueous inclusions from the Yandong porphyry Cu deposit.

high-temperature early ore stage, and hydrostatic pressures in the lower-temperature main ore stage.

6. H–O–S isotopes

The oxygen and hydrogen isotope data are listed in Table 2. The measured $\delta^{18}O$ values of ten quartz samples from different stages range from +6.7 to +9.4‰. Oxygen isotope compositions of the mineralizing hydrothermal fluids were calculated using the quartz-water equilibrium function (Clayton et al., 1972), $1000\ \ln\alpha_{qtz\text{-}water} = 3.38 \times 10^6 \times T^{-2} - 3.40$, based on temperatures obtained by microthermometry of fluid inclusions in the different paragenetic stages of this study (Table 2). Therefore, the calculated $\delta^{18}O$ values of the fluids from stages I to IV are +5.9 to +6.1‰,+1.8 to +2.2‰,+0.3 to +1.0‰, and −6.4‰, respectively (Fig. 13). The δD

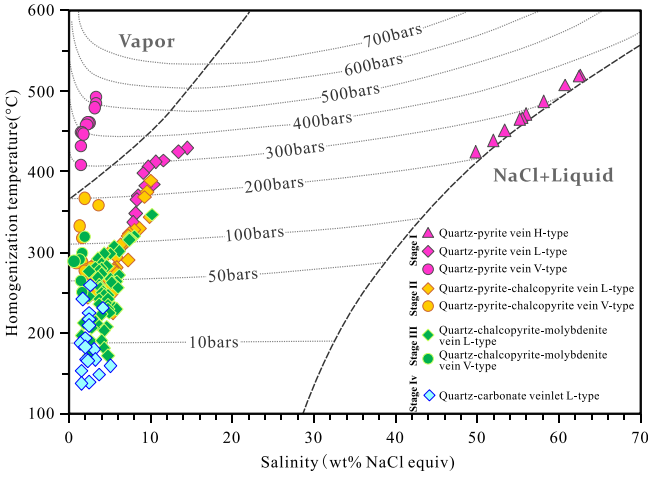

Fig. 12. Pressure estimation for fluid inclusions of the Yandong porphyry Cu deposit. Note that the H-type and V-type inclusions of the quartz ± magnetite ± pyrite stage were trapped under immiscible conditions, and L-type and V-type inclusions of the quartz + pyrite ± chalcopyrite and quartz–polymetallic sulfide stage were trapped under boiling conditions, thus the estimated pressures indicate the actual trapping pressures. Isobars were calculated from the equations of Driesner and Heinrich (2007).

values of fluid inclusion waters of quartz for mineralizing stages I, II, III, and IV are −73 to −68‰, −83 to −82‰, −93 to −76‰, and −78‰, respectively (Fig. 13).

The sulfur isotope data are shown in Table 3 and plotted in Fig. 14. The $\delta^{34}S$ values of nine pyrite samples from the Yandong porphyry Cu deposit range from −2.2 to +0.8‰, with an average of −0.4‰, and the $\delta^{34}S$ values of two chalcopyrite samples are −3.3 and −3.1‰. Therefore, sulfur isotopic compositions in the Yandong deposit show a narrow range ($\delta^{34}S$ = −3.3 to +0.8‰, average = −0.9‰, n = 11), indicating a homogenous sulfur source.

7. Discussion

7.1. Origin of the ore-forming fluids and metals

The isotopic compositions of hydrothermal fluids ($\delta^{18}O$ and δD) are derived from quartz. During the early quartz ± magnetite ± pyrite stage, the $\delta^{18}O$ isotopic compositions calculated for fluids in equilibrium with quartz range from +5.9 to +6.1‰ (average = +6.0‰), which are consistent with fluids derived from magmatic sources (Taylor, 1974; Wang et al., 2013, 2015f). The relatively depleted $\delta^{18}O_{fluids}$ isotopic compositions (+0.3 to +2.2‰) were calculated for fluids of later stages (II and III), possibly due to mixing with some meteoric water. Even the most depleted $\delta^{18}O_{fluid}$ value of about −6.4‰ during the stage IV shows that an important proportion of the fluid is meteoric, assuming that the meteoric paleowater end-member in Tianshan is about −10‰ (Fig. 13; Chen et al., 2012a). In addition, all of the quartz samples at Yandong yielded δD values ranging from −93 to −68‰ (Table 2). These δD ranges indicate the involvement of magmatic fluids in the hydrothermal system, especially in the early stage (Taylor, 1974), similar to those of typical porphyry Cu(–Mo) deposits elsewhere, such as El Salvador Cu deposit in Chile (Sheppard et al., 1976), Toromocho Cu–Mo deposit in Peru (Catchpole et al., 2015), Hugo Dummett Cu deposit in Mongolia (Khashgerel et al., 2009), and Luoboling Cu–Mo deposit in China (Zhong et al., 2014). Alternatively, the shift toward δD and $\delta^{18}O$ depletion from ore stages I to IV (Fig. 13), indicating the evolving nature and source of the hydrothermal fluids, and it is also supported by the results of the fluid inclusion analyses and discussed below.

Table 2
Oxygen and hydrogen isotope data of quartz in the Yandong porphyry Cu deposit.

Sample No.	Mineral	Mineralization stage	T_h (°C)	$\delta^{18}O_{quartz}$(‰)	$\delta^{18}O_{fluid}$(‰)	δD (‰)
YD4703-37	Quartz	Stage I	438	9.4	6.1	−73
YD4703-39	Quartz	Stage I	438	9.2	5.9	−68
YD4703-57	Quartz	Stage II	299	9.1	2.2	−82
YD4703-49	Quartz	Stage II	299	8.7	1.8	−83
YD6307-32	Quartz	Stage III	269	9.1	1.0	−76
YD6307-17	Quartz	Stage III	269	8.7	0.6	−76
YD4703-46	Quartz	Stage III	269	8.6	0.5	−80
YD4703-40	Quartz	Stage III	269	8.4	0.3	−88
YD6307-30	Quartz	Stage III	269	8.4	0.3	−93
YD6307-26	Quartz	Stage IV	179	6.7	−6.4	−78

T_h is the average homogenization temperature of every stage; $\delta^{18}O_{fluid}$ values are calculated according to the quartz-water equilibrium temperature formula provided by Clayton et al. (1972).

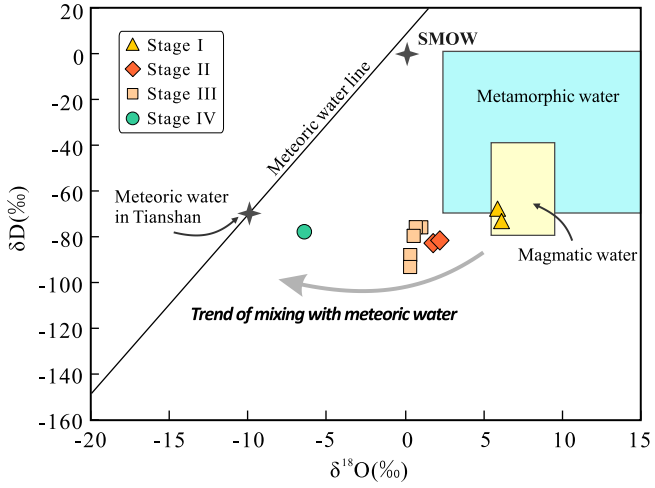

Fig. 13. Plot of $\delta^{18}O$ versus δD, showing the calculated composition for the ore-forming fluids of the Yandong porphyry Cu deposit. Metamorphic water field, magmatic water field, and meteoric water line are from Taylor (1974); meteoric water in Tianshan is from Chen et al. (2012a). SMOW = Standard Mean Ocean Water.

The $\delta^{34}S$ compositions of 11 sulfide samples at Yandong exhibit a narrow $\delta^{34}S$ range of −3.3 to +0.8‰ (Table 3), and overlap with those of porphyry deposits in the Chinese Tianshan and Junggar orogenic belt, such as Tuwu (−3.0 to +1.7‰; Wang et al., 2015a), Yuhai (−1.3 to +0.3‰; Zang, 2014), Yulekenhalasu (−4.5‰ to −0.1‰; Yang et al., 2012a), and Baogutu (−5.1 to +0.7‰; Zhang et al., 2010b). They are also comparable to those of typical porphyry Cu (−Mo) deposits elsewhere, such as Butte Cu–Mo deposit in USA (−0.1 to +4.0‰, Field et al., 2005), Erdenetuin-Obo Cu deposit in Mongolia (−1.8 to +1.5‰; Sotnikov et al., 2004), and Mariquita and Lucky Cu–Mo deposit in Mexico (+0.1 to +3.8‰ and −4.7 to +3.3‰, respectively; Salas et al., 2013) in which ore-forming fluids were inferred to be magmatic in origin. Thus, it is suggested the Yandong Cu deposit has a solely magmatic source of sulfur (−3 to +3‰; Chaussidon et al., 1989), consistent with formation as a porphyry deposit.

In addition, the published whole rock geochemical data (Wang et al., 2015b) of tonalite intrusions at Yandong show that they have high SiO_2 (65–74%) and Al_2O_3 (13–17%) contents, high Sr concentration (129–582 ppm), and low Y and Yb concentrations (5–14 and 0.4–1.2 ppm, respectively), indicating similar geochemical characteristics with adakites (Defant and Drummond, 1990). Most geologists suggest that these adakitic-like rocks were formed in the subduction tectonic setting (Qin et al., 2002; Zhang et al., 2006a; Shen et al., 2014), belonging to island arc granites (Wang et al., 2015a,b; Xiao et al., 2015). The geochemical and Sr–Nd–Hf isotopic signatures of the Yandong tonalite rocks indicate that they were considered to be derived from a subduction oceanic slab with mantle peridotites interaction (Wang et al., 2015b; Xiao et al., 2015), and the ore-forming fluids most likely exsolved from the tonalite magma. In general, associated arc magmas have high magmatic water content, high oxidation states and sulfur content, which are requisites for the formation of magmatic-hydrothermal ore deposits (Richards, 2011; Sun et al., 2015a). Thus, we suggest that the tonalite with arc signatures have the considerably potential to provide ore-forming metals for the Yandong porphyry Cu system.

7.2. Evolution of fluid system and mineralization processes

The evolution of hydrothermal fluid together with its expression in alteration and mineralization in the Yandong deposit is constructed based on petrographic relationships and fluid inclusion microthermometry (Klemm et al., 2008; Catchpole et al., 2011,

Table 3
Sulfur isotope data of sulfides in the Yandong porphyry Cu deposit.

Sample No.	Mineral	Mineralization stage	Sample description	$\delta^{34}S_{V\text{-}CDT}$/‰
YD3104-251-9	Pyrite	Stage I	Py-Mt-Qz vein	−1.3
YD3104-469-18	Pyrite	Stage I	Py-Qz vein	0.1
YD3104-473-20	Pyrite	Stage II	Py-Qz vein	0.6
YD3104-440-7	Pyrite	Stage II	Py-Qz-Cp vein	0.0
YD3104-440-7	Chalcopyrite	Stage II	Py-Qz vein	−3.1
YD3104-46-5	Pyrite	Stage II	Py-Qz-Cp vein	-0.4
YD3104-46-5	Chalcopyrite	Stage II	Py-Qz vein	−3.3
YD3104-484-17	Pyrite	Stage III	Cp-Py-Qz vein	0.8
YD3104-485-19	Pyrite	Stage III	Cp-Py-Qz vein	0.5
YD3104-494-15	Pyrite	Stage III	Py-Qz-Mo vein	−1.7
YD5501-99-2	Pyrite	Stage III	Qz-Cp-Bn-Py vein	−2.2

Mineral abbreviations: Qz = quartz, Py = pyrite, Cp = chalcopyrite, Mt = magnetite, Mo = molybdenite, Bn = bornite.

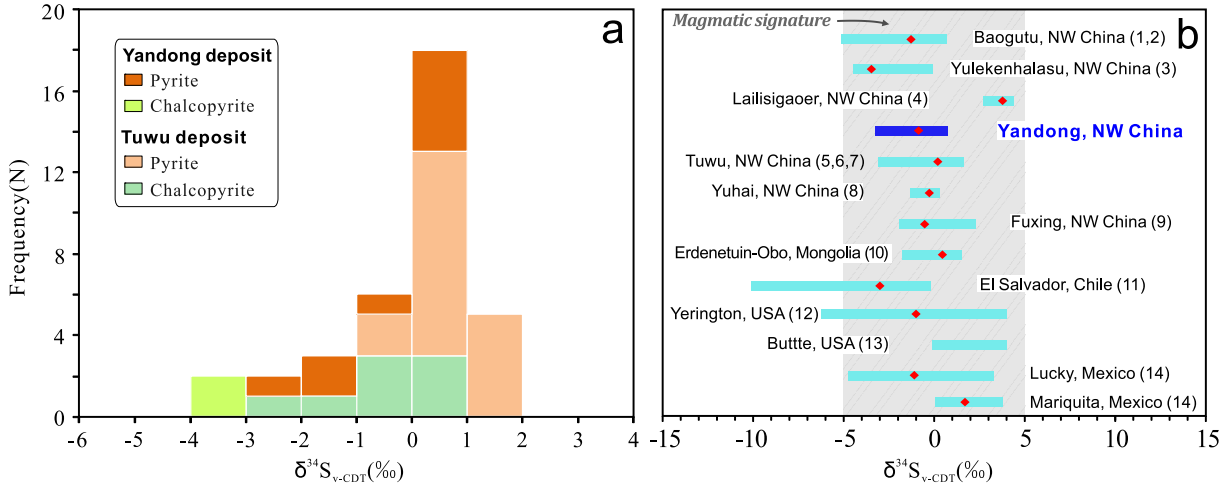

Fig. 14. (a) Histogram of $\delta^{34}S$ values for sulfide minerals from the Yandong porphyry Cu deposit, compared to data from the Tuwu deposit; (b) Sulfur isotope composition of sulfides from Yandong and other porphyry deposits. Data sources: 1, Zhang et al. (2010b); 2, Shen et al. (2012); 3, Yang et al., 2012a; 4, Xue et al. (2011); 5, Wang et al. (2015a); 6, Han et al. (2006); 7, Rui et al. (2002); 8, Zang (2014); 9, Wang et al. (2016d); 10, Sotnikov et al. (2004); 11, Field and Gustafson (1976); 12, Lüders et al. (2009); 13, Field et al. (2005); 14, Salas et al. (2013)

2015). Given the occurrence of the L-, V- and H-types inclusions in the early stage quartz, the initial hydrothermal fluids are characteristic of high salinities (<62.6 wt% NaCl equiv) and homogenization temperatures of 311 to 521 °C. H-type fluid inclusions can only be observed in the early stage, but not in subsequent stages, indicating that the salinity in the fluid decreases gradually due to fluid mixing and/or boiling. Observations of haematite and magnetite (Rui et al., 2002; Zhang et al., 2006a, 2008) in the early stage veins, and the abundance of pyrite and scarcity of pyrrhotite, indicate that the initial hydrothermal fluids were highly oxidized, typical features of porphyry-type deposits (Cooke et al., 2005; Seedorff et al., 2005; Sun et al., 2015b) such as the Bingham Cu deposit, USA (Redmond et al., 2004), the Rosario Cu–Mo deposit, Chile (Masterman et al., 2005), and the Shujiadian Cu deposit, China (Wang et al., 2014b).

Almost H-type fluid inclusions in quartz consistently show homogenization by halite dissolution after bubble disappearance. Such homogenization behavior is relatively common in halite saturated inclusions in magmatic-hydrothermal ore deposits (Roedder, 1971; Nash, 1976; Bouzari and Clark, 2006; Lecumberri-Sanchez et al., 2012). They have been interpreted to be either produced by homogeneous trapping at high pressure (e.g., Roedder and Bodnar, 1980; Baker and Lang, 2003; Masterman et al., 2005), or through a process of post-entrapment modification (e.g., Klemm et al., 2008), or else, direct exsolution from the parent magma (e.g., Cline and Bodnar, 1994; Zhang et al., 2007; Lecumberri-Sanchez et al., 2015). Given that the high-pressure trapping is limited to deposits formed at deeper crustal levels (Lecumberri-Sanchez et al., 2015), we can thus rule out this interpretation for the H-type fluid inclusions. The analyzed fluid inclusion assemblages showed no petrographic evidence of post-entrapment disturbance. Besides, halite homogenization at temperatures well above homogenization of the bubble in H-type inclusions do not yield unreasonably high trapping temperatures, implying that significant modification process may not occur. Furthermore, Lecumberri-Sanchez et al. (2015) have pointed out that the coexistence of H-type inclusions that homogenize by halite disappearance with vapor-rich inclusions would be a direct consequence of halite saturation along the liquid-vapor-halite curve, which have been documented in most porphyry-type ore-forming systems (e.g., Bodnar and Beane, 1980; Muntean and Einaudi, 2001; Lecumberri-Sanchez et al., 2012). Therefore, we suggest that the H-type fluid inclusions at Yandong were most likely trapped under halite-saturated conditions released from a silicate melt.

Combined with the H–O stable isotope data presented above, it can be concluded that the fluids have evolved from magmatic hydrothermal to meteoric in origin. As the Yandong porphyry intrusions cooled and crystallized, we suggest that an initially supercritical fluid exsolved from the parental magma chamber, at shallow levels (~5 km) in the earth's crust (pressures of 1.1–1.2 kbar) (Burnham, 1979; Hedenquist and Lowenstern, 1994). Fluid exsolved from this magma was rich in K, F and most likely Cu and was marked by high temperature, high salinity, and high oxygen fugacity. Rapid ascent to a depth of ~1 km (~300 bars) caused the fluid to intersect its solvus at a temperature of ~400 to 500 °C and to generate immiscible hypersaline liquid phase (~56 wt% NaCl equiv; Fig. 12) and a low-density vapor (Driesner and Heinrich, 2007), as is indicated by the coexistence of V-type and H-type inclusions in the quartz–magnetite–pyrite veins. The fluid filtered through and reacted with the porphyry complex and/or wall rock, resulting in the alteration assemblage of K-feldspar, quartz, and minor biotite, with the formation of quartz ± pyrite ± magnetite veins during the early stage.

As magma solidification advances downward, the entire magmatic-hydrothermal system progressively cooled and diluted, with homogenization temperatures of 161 to 390 °C and salinities of <9.9 wt% NaCl equiv during the ore stages II and III (Fig. 10). The rock can fracture in a brittle fashion on cooling below ~400 °C (Fournier, 1987, 1999; Sillitoe, 2010). Therefore, lithostatic gives way to hydrostatic pressure, and erosion (or some other mechanism) progressively degrades the paleosurface during the main ore stage (Sillitoe, 2010). Under these temperatures and pressure conditions, chlorite-sericite and phyllic alteration zones begun to form that overprinted the early hydrothermal assemblages, and the chlorite-sericite and phyllic alteration would have produced significant porphyry Cu ± Au mineralization in and around the central porphyry body at Yandong (Landtwing et al., 2005; Shen et al., 2014; Wang et al., 2015b). Fluid inclusions in the late ore stage (IV) quartz only contain L-type, characterized by lower homogenization temperatures (average = 179 °C) and salinities (average = 2.0 wt% NaCl equiv; Fig. 10), indicating the involvement of external meteoric water in the fluid system. Along with meteoric water input at the shallow crust, the metal contents and solubility are decreased, whereas the oxidizability are enhanced, finally causing the development of quartz–calcite veins and minor mineralization.

A variety of ore deposition processes might be invoked at Yandong. Firstly, temperature decreased from 310–520 °C in the early ore stage I to 160–390 °C in the main ore stage (II and III), with a sharp decrease in salinity from ~60 wt% to ~10 wt% (Table 1; Fig. 10). Experimental studies indicate that Cu solubility decreases with decreasing temperature and salinity (Redmond et al., 2004; Landtwing et al., 2005). Secondly, the PH value of ore-forming fluid would have increased by reaction with the country rocks, which would reduce the solubility of Cu (Brimhall and Crerar, 1987). Additionally, fluid boiling is suggested to have occurred in the main ore stage (II and III); phase separation would increase the Cu concentration in the ore-forming fluid (Harris et al., 2003). Geochemical modeling based on LA-ICP-MS analysis of fluid inclusions may assess what the most important mechanisms are for precipitation (Bertelli et al., 2009; Zhu et al., 2015), but the available data suggest the ore deposition could be readily initiated by all of processes above in concert.

7.3. Remarks on possible magmatic-hydrothermal origin

We propose that the ore-forming fluids and ore metals were derived from an oxidized magmatic system, based on the metal signature, mineral association, fluid characteristic, isotopic evidence, and tectonomagmatic setting of the Yandong deposit. The ductile shear faults and breccias developed in the area also indicated that the faults and breccias acted as pathways for upward flow of deep-seated ore-forming fluids.

Hypogene bornite and rutile are typical magmatic-hydrothermal minerals related to magmatic fluids (Einaudi et al., 2003), and commonly occur in magmatic-hydrothermal systems, such as porphyry and epithermal deposits (e.g., Einaudi et al., 2003; Cooke et al., 2005; Wang et al., 2014a; Jian et al., 2015), and porphyry Cu deposits are generally associated with oxidized magmatic systems rather than reduced magmatic systems (Lehmann, 1990; Seedorff et al., 2005; Sun et al., 2014). The oxidized fluid environment of the Yandong deposit is indicated by the mineral association, such as the presence of anhydrite in ore stage II, the abundance of hematite and magnetite and scarcity of pyrrhotite (Rui et al., 2002; Zhang et al., 2006a, 2008), and the presence of biotite in tonalite (Mg/(Mg + Fe + Mn) values ranging from 0.35 to 0.60; Zhang et al., 2006a; Wang et al., 2015b). In addition, reduced gases such as CH_4 and N_2 were not detected in fluid inclusions by Raman spectroscopic analysis.

A magmatic-hydrothermal origin is in accordance with the local tectonomagmatic setting. The Early Carboniferous is an important magmatic period in eastern Tianshan orogenic belt, with abundant intermediate to felsic intrusions (e.g. Tuwu tonalite,~332 Ma, Wang et al., 2015a, Chihu tonalite, ~320 Ma, Zhang et al., 2016a) emplaced in a subduction-related collision setting, and related to partial melting of the subducted Palaeo-Tianshan oceanic slab beneath the southern margin of the Dananhu-Tousuquan arc belt (Mao et al., 2005; Zhang et al., 2006a; Wang et al., 2015a,b). Similarly, the parent magma of the Yandong porphyry Cu deposit may stem from partial melting of subducted oceanic slab, given that Sr and Nd isotope data of the host rocks and ore sulfides plot near the subduction-related adakites ranging along the mantle array (Zhang et al., 2006a,b). Because H_2O, SO_2, and other volatiles derived from devolatilization of the oceanic slab would have metasomatized the overlying mantle wedge, melting of the subducted oceanic slab mixed with this enriched mantle wedge could produce magmas with high H_2O and SO_2 contents and, thus, high oxygen fugacity (Sillitoe, 2010). On crystallization of oxidized magmas, Cu, Au, and S preferentially partition into the silicate liquid (Candela, 1992; Jugo et al., 1999), thus producing Cu-rich residual melts with subsequent removal of Cu into the vapor phase (Heinrich, 2005; Seo et al., 2009, 2012). Then upward decompression and expansion of the vapor phase, accompanied by temperature decreasing, causes rapidly decreasing solubility of the vapor-transported metals (Hedenquist et al., 1998; Williams-Jones et al., 2002; Sillitoe, 2010), at relatively shallow levels in the earth's crust (~1 km). Such a decrease in solubility resulted in wholesale precipitation of the Cu sulfides together with minor Au, thus potentially contributing to a large proportion of Cu mineralization at Yandong. In addition, crustal fracture systems associated with northward subduction served as ideal environment for ore-forming fluid flow and accumulation.

8. Conclusions

1) The Yandong Cu deposit in eastern Tianshan has mineral associations, related alteration and styles of mineralization similar to typical porphyry deposits elsewhere. Its hydrothermal process includes four stages: an early quartz ± magnetite ± pyrite stage (I), a quartz + pyrite ± chalcopyrite stage (II), a quartz + chalcopyrite ± pyrite ± molybdenite stage (III), and a late quartz + carbonate stage (IV).
2) Hydrothermal quartz from the Yandong Cu deposit mainly contains three types of fluid inclusions, namely two-phase liquid-rich, two-phase vapor-rich and three-phase hypersaline inclusions. The initial hydrothermal fluid is a H_2O–NaCl system with high temperature, high salinity and high oxygen-fugacity.
3) Hydrogen and oxygen isotopic data indicate that the ore-forming fluids of the Yandong deposit have evolved from magmatic hydrothermal to meteoric in origin. Sulfur isotopic signatures suggest that ore-forming metals were primarily originated from the tonalite magma with its source in the subducted oceanic crust and some mantle materials.
4) The Yandong deposit is associated with oxidized magmatic system with mineralization depth of approximately 1 km. Fluid boiling or phase separation, decrease of temperature, as well as fluid-rock interaction are important factors responsible for metal accumulation and deposition in the magmatic-hydrothermal system.

Acknowledgments

This research was jointly funded by the National Natural Science Foundation of China (41572066), the Fundamental Research Funds of the Central Universities (2652015019 and 2652015032), and the Geological Survey Project of China (1212011085471 and 1212011220923). We are very grateful to the Editor-in-Chief Franco Pirajno and two reviewers for their constructive comments and assistance in improving the manuscript. We thank Lian-Hui Dong and Jing Feng from the Xinjiang Bureau of Geology and Mineral Exploration for their great support and assistance in our fieldwork. We also appreciate the kind help of Li Liu from China University of Geosciences at Beijing (CUGB) on the fluid inclusion microthermometric measurements and Raman spectroscopic analysis. We thank Professor Yu-Sheng Zhai from CUGB for a helpful scientific review of the original manuscript.

References

Baker, T., Lang, J.R., 2003. Reconciling fluid inclusions, fluid processes and fluid source in skarns: an example from the Bismark skarn deposit, Mexico. Miner. Deposita 38, 474–495.
Bertelli, M., Baker, T., Cleverley, J.S., Ulrich, T., 2009. Geochemical modelling of a Zn-Pb skarn: constraints from LA-ICP-MS analysis of fluid inclusions. J. Geochem. Explor. 102, 13–26.
Bodnar, R.J., 1993. Revised equation and table for determining the freezing point depression of H_2O-NaCl solutions. Geochim. Cosmochim. Acta 57, 683–684.

Bodnar, R.J., Beane, R.E., 1980. Temporal and spatial variations in hydrothermal fluid characteristics during vein filling in preore cover overlying deeply buried porphyry copper-type mineralization at Red Mountain, Arizona. Econ. Geol. 75, 876–893.
Bouzari, F., Clark, A.H., 2006. Prograde evolution and geothermal affinities of a major porphyry copper deposit: the Cerro Colorado Hypogene Protore, I Región, Northern Chile. Econ. Geol. 101, 95–134.
Brimhall, G.H., Crerar, D.A., 1987. Ore fluids: magmatic to supergene. Rev. Mineral. Geochem. 17, 235–321.
Burnham, C.W., 1979. Magmas and hydrothermal fluids. In: Barnes, H.L. (Ed.), Geochemistry of hydrothermal ore deposits. second ed. John Wiley and Sons, New York, pp. 71–136.
Candela, P.A., 1992. Controls on ore metal ratios in granite-related ore systems: an experimental and computational approach. Trans. R. Soc. Edinburgh. Earth Sci. 83, 317–326.
Catchpole, H., Kouzmanov, K., Fontboté, L., Guillong, M., Heinrich, C.A., 2011. Fluid evolution in zoned Cordilleran polymetallic veins - Insights from microthermometry and LA-ICP-MS of fluid inclusions. Chem. Geol. 281, 293–304.
Catchpole, H., Kouzmanov, K., Putlitz, B., Seo, J.H., Fontboté, L., 2015. Zoned base metal mineralization in a porphyry system: origin and evolution of mineralizing fluids in the Morococha district, Peru. Econ. Geol. 110, 39–71.
Charvet, J., Shu, L.S., Charvet, S.L., 2007. Paleozoic structural and geodynamic evolution of eastern Tianshan (NW China): welding of the Tarim and Junggar plates. Episodes 30, 162–186.
Chaussidon, M., Albarede, F., Sheppard, S.M.F., 1989. Sulphur isotope variations in the mantle from ion microprobe analyses of micro-sulphide inclusions. Earth Planet. Sc. Lett. 92, 144–156.
Chen, F.W., Li, H.Q., Chen, Y.C., Wang, D.H., Wang, J.L., Liu, D.Q., Tang, Y.L., Zhou, R.H., 2005. Zircon SHRIMP U-Pb dating and its geological significance of mineralization in Tuwu-Yandong porphyry copper mine, East Tianshan Mountain. Acta Geol. Sin. 2, 247–254 (in Chinese with English abstract).
Chen, X.H., Qu, W.J., Han, S.Q., Eleonora, S., Yang, N., Chen, Z.L., Zeng, F.G., Du, A.D., Wang, Z.H., 2010. Re-Os geochronology of Cu and W-Mo deposits in the Balkhash metallogenic belt, Kazakhstan and its geological significance. Geosci. Front. 1, 115–124.
Chen, X.J., Shu, L.S., Santosh, M., 2011. Late Paleozoic post-collisional magmatism in the Eastern Tianshan belt, northwest China: new insights from geochemistry, geochronology and petrology of bimodal volcanic rocks. Lithos 127, 581–598.
Chen, H.Y., Yang, J.T., Baker, M., 2012a. Mineralization and fluid evolution of the Jiyuan polymetallic Cu–Ag–Pb–Zn–Au deposit, Eastern Tianshan, NW China. Int. Geol. Rev. 54, 816–832.
Chen, Y.J., Pirajno, F., Wu, G., Qi, J.P., Xiong, X.L., 2012b. Epithermal deposits in North Xinjiang, NW China. Int. J. Earth Sci. 101, 889–917.
Clayton, W.M., Mayeda, T.K., 1963. The use of bromine pent a fluoride in the extraction of oxygen from oxides and silicates for isotopic analysis. Geochim. Cosmochim. Acta 27, 43–52.
Clayton, R.N., O'Neil, J.L., Meyeda, T.K., 1972. Oxygen isotope exchange between quartz and water. J. Geophys. Res. 77, 3057–3067.
Cline, J.S., Bodnar, R.J., 1994. Direct evolution of brine from a crystallizing silicic melt at the Questa, New Mexico, molybdenum deposit. Econ. Geol. 89, 1780–1802.
Cooke, D.R., Hollings, P., Walshe, J.L., 2005. Giant porphyry deposits: characteristics, distribution, and tectonic controls. Econ. Geol. 100, 801–818.
Defant, M.J., Drummond, M.S., 1990. Derivation of some modern arc magmas by melting of young subducted lithosphere. Nature 347, 662–665.
Deng, J., Wang, Q.F., 2015. Gold mineralization in China: metallogenic provinces, deposit types and tectonic framework. Gondwana Res. http://dx.doi.org/10.1016/j.gr.2015.10.003.
Deng, J., Wang, Q.F., Li, G.J., Santosh, M., 2014. Cenozoic tectono-magmatic and metallogenic processes in the Sanjiang region, southwestern China. Earth Sci. Rev. 138, 268–299.
Deng, J., Wang, Q.F., Li, G.J., Zhao, Y., 2015a. Structural control and genesis of the Oligocene Zhenyuan orogenic gold deposit, SW China. Ore Geol. Rev. 65, 42–54.
Deng, Y.F., Yuan, F., Zhou, T.F., Xu, C., Zhang, D.Y., Guo, X.J., 2015b. Geochemical characteristics and tectonic setting of the Tuerkubantao mafic-ultramafic intrusion in West Junggar, Xinjiang, China. Geosci. Front. 6, 141–152.
Driesner, T., Heinrich, C.A., 2007. The system H2O-NaCl. Part I: correlation formulae for phase relations in temperature-pressure-composition space from 0 to 1000 C, 0 to 5000 bar, and 0 to 1 XNaCl. Geochim. Cosmochim. Acta 71, 4880–4901.
Einaudi, M.T., Hedenquist, J., Inan, E., 2003. Sulfidation state of fluids in active and extinct hydrothermal systems: transitions from porphyry to epithermal environments. Soc. Econ. Geol. Spec. Publ. 10, 285–313.
Field, C.W., Gustafson, L.B., 1976. Sulfur isotopes in the porphyry copper deposit at El Salvador, Chile. Econ. Geol. 71, 1533–1548.
Field, C.W., Zhang, L., Dilles, J.H., Rye, R.O., Reed, M.H., 2005. Sulfur and oxygen isotope record in sulfate and sulfide minerals of early, deep, pre-Main Stage porphyry Cu-Mo and late Main Stage base-metal mineral deposits, Butte district. Montana. Chem. Geol. 215, 61–93.
Fournier, R.O., 1987. Conceptual Models of Brine Evolution in Magmatic Hydrothermal Systems. U.S. Geol. Surv. Prof. Paper 1350, 1487–1506.
Fournier, R.O., 1999. Hydrothermal process related to movement of fluid from plastic into brittle rock in the magmatic–epithermal environment. Econ. Geol. 94, 1193–1211.
Gao, J.F., Zhou, M.F., Qi, L., Chen, W., Huang, X.W., 2015. Chalcophile elemental compositions and origin of the Tuwu porphyry Cu deposit, NW China. Ore Geol. Rev. 66, 403–421.
Goldfarb, R.J., Taylor, R.D., Collins, G.S., Goryachev, N.A., Orlandini, O.F., 2014. Phanerozoic continental growth and gold metallogeny of Asia. Gondwana Res. 25, 48–102.
Han, C.M., Xiao, W.J., Zhao, G.C., Mao, J.W., Li, S.Z., Yan, Z., Mao, Q.G., 2006. Major types, characteristics and geodynamic mechanism of upper Paleozoic copper deposits in northern Xinjiang, north western China. Ore Geol. Rev. 28, 308–328.
Harris, A.C., Kamenetsky, V.S., White, N.C., Van Achterbergh, E., Ryan, C.G., 2003. Melt inclusions in veins: linking magmas and porphyry Cu deposits. Science 302, 2109–2111.
Hedenquist, J.W., Lowenstern, J.B., 1994. The role of magmas in the formation of hydrothermal ore deposits. Nature 370, 519–527.
Hedenquist, J.W., Arribas, A., Reynolds, T.J., 1998. Evolution of intrusion-centered hydrothermal system: far Southeast-Lepanto porphyry and epithermal Cu-Au deposits, Philippines. Econ. Geol. 93, 373–404.
Heinrich, C.A., 2005. The physical and chemical evolution of low-salinity magmatic fluids at the porphyry to epithermal transition: a thermodynamic study. Miner. Deposita 39, 864–889.
Hou, G.S., Tang, H.F., Liu, C.Q., Wang, Y.B., 2005. Geochronological and geochemical study on the wall rock of Tuwu-Yandong porphyry copper deposits, Eastern Tianshan Mountains. Acta Petrol. Sin. 21, 1729–1736 (in Chinese with English abstract).
Hou, T., Zhang, Z.C., Santosh, M., Encarnacion, J., Zhu, J., Luo, W.J., 2014. Geochronology and geochemistry of submarine volcanic rocks in the Yamansu iron deposit, Eastern Tianshan Mountains, NW China: constraints on the metallogenesis. Ore Geol. Rev. 56, 487–502.
Huang, X.W., Qi, L., Gao, J.F., Zhou, M.F., 2013. First reliable Re–Os Ages of pyrite and stable isotope compositions of Fe(-Cu) deposits in the Hami Region, Eastern Tianshan Orogenic Belt, NW China. Resour. Geol. 63, 166–187.
Jia, Z.Y., Xue, C.J., Qu, W.J., Zhao, Q., Zhang, Q., 2011. Geology, S, Pb, O and H isotopic compositions and Re-Os chronology of Kendenggaoer Cu-Mo deposit in Xinjiang. Miner. Depos. 30, 74–86 (in Chinese with English abstract).
Jian, W., Lehmann, B., Mao, J.W., Ye, H.S., Li, Z.Y., He, H.J., Zhang, J.E., Zhang, H., Feng, J.W., 2015. Mineralogy, fluid Characteristics, and Re-Os Age of the Late Triassic Dahu Au-Mo Deposit, Xiaoqinling Region, Central China: evidence for a Magmatic-Hydrothermal Origin. Econ. Geol. 110, 119–145.
Jugo, P.J., Candela, P.A., Piccoli, P.M., 1999. Magmatic sulfides and Au: Cu ratios in porphyry deposits: an experimental study of copper and gold partitioning at 850 C, 100 MPa in a haplogranitic melt-pyrrhotite-intermediate solid solution-gold metal assemblage, at gas saturation. Lithos 46, 573–589.
Khashgerel, B.E., Rye, R.O., Kavalieris, I., Hayashi, K.I., 2009. The sericitic to advanced argillic transition: stable isotope and mineralogical characteristics from the Hugo Dummett porphyry Cu-Au deposit, Oyu Tolgoi District, Mongolia. Econ. Geol. 104, 1087–1110.
Klemm, L.M., Pettke, T., Heinrich, C.A., 2008. Fluid and source magma evolution of the Questa porphyry Mo deposit, New Mexico, USA. Miner. Deposita 43, 533–552.
Kovalenko, V.I., Yarmolyuk, V.V., Kovach, V.P., Kotov, A.B., Kozakov, I.K., Salnikova, E. B., Larin, A.M., 2004. Isotope provinces, mechanisms of generation and sources of the continental crust in the Central Asian mobile belt: geological and isotopic evidence. J. Asian Earth Sci. 23, 605–627.
Landtwing, M.R., Pettke, T., Halter, W.E., Heinrich, C.A., Redmond, P.B., Einaudi, M.T., Kunze, K., 2005. Copper deposition during quartz dissolution by cooling magmatic–hydrothermal fluids: the Bingham porphyry. Earth Planet. Sc. Lett. 235, 229–243.
Lecumberri-Sanchez, P., Steele-MacInnis, M., Bodnar, R.J., 2012. A numerical model to estimate trapping conditions of fluid inclusions that homogenize by halite disappearance. Geochim. Cosmochim. Acta 92, 14–22.
Lecumberri-Sanchez, P., Steele-MacInnis, M., Weis, P., Driesner, T., Bodnar, R.J., 2015. Salt precipitation in magmatic-hydrothermal systems associated with upper crustal plutons. Geology 43, 1063–1066.
Lehmann, B., 1990. Metallogeny of tin. Springer-Verlag, Berlin-Heidelberg-New York, p. 211.
Li, D., He, D.F., Fan, C., 2015. Geochronology and Sr-Nd-Hf isotopic composition of the granites, enclaves, and dikes in the Karamay area, NW China: insights into late Carboniferous crustal growth of West Junggar. Geosci. Front. 6, 153–173.
Lüders, V., Romer, R.L., Gilg, A.H., Bodnar, R.J., Pettke, T., Misantoni, D., 2009. A geochemical study of the Sweet Home mine, Colorado Mineral Belt, USA: hydrothermal fluid evolution above a hypothesized granite cupola. Miner. Deposita 44, 415–434.
Mao, S., Duan, Z., 2008. The P, V, T, x properties of binary aqueous chloride solutions up to T = 573 K and 100 MPa. J. Chem. Thermodyn. 40, 1046–1063.
Mao, J.W., Goldfarb, R.T., Wang, Y.T., Hart, C.J., Wang, Z.L., Yang, J.M., 2005. Late Paleozoic base and precious metal deposits, East Tianshan, Xinjiang, China, characteristics and geodynamic setting. Episodes 28, 1–14.
Mao, Y.J., Qin, K.Z., Li, C., Tang, D.M., 2015. A modified genetic model for the Huangshandong magmatic sulfide deposit in the Central Asian Orogenic Belt, Xinjiang, western China. Miner. Deposita 50, 65–82.
Masterman, G.J., Cooke, D.R., Berry, R.F., 2005. Fluid chemistry, structural setting, and emplacement history of the Rosario Cu–Mo porphyry and Cu–Ag–Au epithermal veins, Collahuasi District, Northern Chile. Econ. Geol. 100, 835–862.
Muntean, J.L., Einaudi, M.T., 2001. Porphyryepithermal transition: Maricunga belt, northern Chile. Econ. Geol. 96, 743–772.

Nash, T.J., 1976. Fluid-inclusion petrology-Data from porphyry copper deposits and applications to exploration. U.S. Geological Survey Professional Paper 907-D, p. 16.
Pirajno, F., 2010. Intracontinental strike-slip faults, associated magmatism, mineral systems and mantle dynamics: examples from NW China and Altay-Sayan (Siberia). J. Geodyn. 50, 325–346.
Pirajno, F., Seltmann, R., Yang, Y.Q., 2011. A review of mineral systems and associated tectonic settings of northern Xinjiang, NW China. Geosci. Front. 2, 157–185.
Porter, T.M., 2016. The geology, structure and mineralisation of the Oyu Tolgoi porphyry copper-gold-molybdenum deposits, Mongolia: a review. Geosci. Front. 7, 375–407.
Qin, K.Z., Fang, T.H., Wang, S.L., Zhu, B.Q., Feng, Y.M., Yu, H.F., Xiu, Q.Y., 2002. Plate tectonic division, evolution and metallogenic settings in eastern Tianshan Mountains: NW China. Xinjiang Geol. 20, 302–308 (in Chinese with English abstract).
Redmond, P.B., Einaudi, M.T., Inan, E.E., Landtwing, M.R., Heinrich, C.A., 2004. Copper deposition by fluid cooling in intrusion-centered systems: new insights from the Bingham porphyry ore deposits, Utah. Geology 32, 217–220.
Richards, J.P., 2011. High Sr/Y arc magmas and porphyry Cu ± Mo ± Au deposits: just add water. Econ. Geol. 106, 1075–1081.
Roedder, E., 1971. Fluid inclusion studies on the porphyry-type ore deposits at Bingham, Utah, Butte, Montana, and Climax, Colorado. Econ. Geol. 66, 98–118.
Roedder, E., 1984. Fluid inclusions. Rev. Mineral. 12, 644.
Roedder, E., Bodnar, R., 1980. Geologic pressure determinations from fluid inclusion studies. Annu. Rev. Earth Planet. Sci. 8, 263–301.
Rui, Z.Y., Wang, L.S., Wang, Y.T., Liu, Y.L., 2002. Discussion on metallogenic epoch of Tuwu and Yandong porphyry copper deposits in East Tianshan Mountains, Xinjiang. Miner. Depos. 21, 16–22 (in Chinese with English abstract).
Salas, R.D.R., Ochoa-Landín, L., Ruiz, J., Eastoe, C., Meza-Figueroa, D., Zuniga-Hernandez, H., Mendívil-Quijada, H., Quintanar-Ruiz, F., 2013. Geology, stable isotope, and U-Pb geochronology of the Mariquita porphyry copper and Lucy Cu-Mo deposits, Cananea district, Mexico: a contribution to regional exploration. J. Geochem. Explor. 124, 140–154.
Seedorff, E., Dilles, J.H., Proffett, J.M., Jr., Einaudi, M.T., Zurcher, L., Stavast, W.J.A., Johnson, D.A., Barton, M.D., 2005. Porphyry deposits: Characteristics and origin of hypogene features. Economic Geology 100th Anniversary Volume, 251–298.
Seltmann, R., Porter, T.M., Pirajno, F., 2014. Geodynamics and metallogeny of the central Eurasian porphyry and related epithermal mineral systems. A review. J. Asian Earth Sci. 79 (Part B), 810–841.
Sengor, A.M.C., Natal'In, B.A., Burtman, V.S., 1993. Evolution of the Altaid tectonic collage and Palaeozoic crustal growth in Eurasia. Nature 364, 299–307.
Seo, J.H., Guillong, M., Heinrich, C.A., 2009. The role of sulfur in the formation of magmatic-hydrothermal copper-gold deposits. Earth Planet. Sc. Lett. 282, 323–328.
Seo, J.H., Guillong, M., Heinrich, C.A., 2012. Separation of molybdenum and copper in porphyry deposits: the roles of sulfur, redox, and pH in ore mineral deposition at Bingham Canyon. Econ. Geol. 107, 333–356.
Shen, P., Shen, Y.H., Pan, H.D., Li, X.H., Dong, L.H., Wang, J.B., Zhu, H.P., Dai, H.W., Guan, W.N., 2012. Geochronology and isotope geochemistry of the Baogutu porphyry copper deposit in the West Junggar region, Xinjiang, China. J. Asian Earth Sci. 49, 99–115.
Shen, P., Pan, H.D., Dong, L.H., 2014. Yandong porphyry Cu deposit, Xinjiang, China-Geology, geochemistry and SIMS U-Pb zircon geochronology of host porphyries and associated alteration and mineralization. J. Asian Earth Sci. 80, 197–217.
Shen, P., Pan, H.D., Shen, Y.C., Yan, Y.H., Zhong, S.H., 2015. Main deposit styles and associated tectonics of the West Junggar region, NW China. Geosci. Front. 6, 175–190.
Sheppard, S.M.F., Gustafson, L.B., Sheppard, S.M.F., 1976. Oxygen and hydrogen isotopes in the porphyry copper deposit at El Salvador, Chile. Econ. Geol. 71, 1549–1559.
Sillitoe, R.H., 2010. Porphyry copper systems. Econ. Geol. 105, 3–41.
Singer, D.A., Berger, V.I., Moring, B.C., 2008. Porphyry copper deposits of the world: Database and grade and tonnage models, 2008. U.S. Department of the Interior, U.S. Geological Survey, Open-File, Report 2008–1155.
Sotnikov, V.I., Ponomarchuk, V.A., Pertseva, A.P., Berzina, A.P., Berzina, A.N., Gimon, V.O., 2004. Evolution of sulfur isotopes in porphyry Cu-Mo ore-magmatic systems of Siberia and Mongolia. Russ. Geol. Geophys. 45, 963–974.
Sterner, S.M., Hall, D.L., Bodnar, R.J., 1988. Synthetic fluid inclusions. V. Solubility relations in the system NaCl-KCl-H_2O under vapor-saturated conditions. Geochim. Cosmochim. Acta 52, 989–1005.
Su, B.X., Qin, K.Z., Sun, H., Tang, D.M., Xiao, Q.H., Liu, P.P., 2012. Olivine compositional mapping of mafic-ultramafic complexes in Eastern Xinjiang (NW China): implications for Cu–Ni mineralization and tectonic dynamics. J. Earth Sci. 23, 41–53.
Sun, W.D., Huang, R.F., Liang, H.Y., Ling, M.X., Li, G.Y., Ding, X., Zhang, H., Yang, X.Y., Ireland, T., Fan, W.M., 2014. Magnetite–hematite, oxygen fugacity, adakite and porphyry copper deposits: reply to Richards. Geochim. Cosmochim. Acta 126, 646–649.
Sun, W.D., Ding, X., Ling, M.X., Zartman, R.E., Yang, X.Y., 2015a. Subduction and ore deposits. Int. Geol. Rev. 57, 9–10.
Sun, H.R., Huang, Z.L., Li, W.B., Ye, L., Zhou, J.X., 2015b. Geochronological, isotopic and mineral geochemical constraints on the genesis of the Diyanqinamu Mo deposit, Inner Mongolia, China. Ore Geol. Rev. 65, 70–83.
Taylor, H.P., 1974. The application of oxygen and hydrogen isotope studies to problems of hydrothermal alteration and ore deposition. Econ. Geol. 69, 843–883.
Wan, B., Xiao, W.J., Han, C.M., Windley, B.F., Zhang, L.C., Qu, W.J., Du, A.D., 2015. Re–Os molybdenite age of the Cu–Mo skarn ore deposit at Suoerkuduke in East Junggar, NW China and its geological significance. Ore Geol. Rev. 56, 541–548.
Wang, Y.H., Zhang, F.F., 2016. Petrogenesis of early Silurian intrusions in the Sanchakou area of Eastern Tianshan, Northwest China, and tectonic implications: geochronological, geochemical, and Hf isotopic evidence. Int. Geol. Rev. 58, 1294–1310.
Wang, C.M., He, X.Y., Yan, C.H., Lü, W.D., Sun, W.Z., 2013. Ore Geology, and H, O, S, Pb, Ar isotopic constraints on the genesis of the Lengshuibeigou Pb–Zn–Ag deposit, China. Geos. J. 17, 197–210.
Wang, C.M., Zhang, D., Wu, G.G., Santosh, M., Zhang, J., Xu, Y.G., Zhang, Y.Y., 2014a. Geological and isotopic evidence for magmatic-hydrothermal origin of the Ag–Pb–Zn deposits in the Lengshuikeng District, east-central China. Miner. Deposita 49, 733–749.
Wang, S.W., Zhou, T.F., Yuan, F., Fan, Y., White, N.C., Lin, F.J., 2014b. Geological and geochemical studies of the Shujiadian porphyry Cu deposit, Anhui Province, Eastern China: implications for ore genesis. J. Asian Earth Sci. 103, 252–275.
Wang, Y.H., Xue, C.J., Liu, J.J., Wang, J.P., Yang, J.T., Zhang, F.F., Zhao, Z.N., Zhao, Y.J., Liu, B., 2015a. Early Carboniferous adakitic rocks in the area of the Tuwu deposit, eastern Tianshan, NW China: slab melting and implications for porphyry copper mineralization. J. Asian Earth Sci. 103, 332–349.
Wang, Y.H., Xue, C.J., Wang, J.P., Peng, R.M., Yang, J.T., Zhang, F.F., Zhao, Z.N., Zhao, Y.J., 2015b. Petrogenesis of magmatism in the Yandong region of Eastern Tianshan, Xinjiang: geochemical, geochronological and Hf isotope Constraints. Int. Geol. Rev. 57, 1130–1151.
Wang, Y.H., Xue, C.J., Zhang, F.F., Liu, J.J., Gao, J.B., Qi, T.J., 2015c. SHRIMP zircon U-Pb geochronology, geochemistry and H-O-Si-S-Pb isotope systematics of the Kanggur gold deposit in Eastern Tianshan, NW China: implication for ore genesis. Ore Geol. Rev. 68, 1–13.
Wang, Y.H., Zhang, F.F., Liu, J.J., Xue, C.J., Wang, J.P., Liu, B., Lu, W.W., 2015d. Petrogenesis of granites in Baishan molybdenum deposit, eastern Tianshan, Xinjiang: Zircon U-Pb geochronology, geochemistry, and Hf isotope constraints. Acta Petrol. Sin. 31, 1962–1976 (in Chinese with English abstract).
Wang, Y.H., Zhao, C.B., Zhang, F.F., Liu, J.J., Wang, J.P., Peng, R.M., Liu, B., 2015e. SIMS zircon U-Pb and molybdenite Re–Os geochronology, Hf isotope, and whole-rock geochemistry of the Wunugetushan porphyry Cu–Mo deposit and granitoids in NE China and their geological significance. Gondwana Res. 28, 1228–1245.
Wang, C.M., Deng, J., Santosh, M., Carranza, Emmanuel John M., Gong, Q.J., Guo, C.Y., Xia, R., Lai, X.R., 2015f. Timing, tectonic implications and genesis of gold mineralization in the Xincheng gold deposit, China: C-H-O isotopes, pyrite Rb-Sr and zircon fission track thermochronometery. Ore Geol. Rev. 65, 659–673.
Wang, Y.H., Xue, C.J., Liu, J.J., Zhang, F.F., 2016a. Geological, geochronological, geochemical, and Sr–Nd–O–Hf isotopic constraints on origins of intrusions associated with the Baishan porphyry Mo deposit in eastern Tianshan, NW China. Miner. Deposita 51, 953–969.
Wang, Y.H., Xue, C.J., Gao, J.B., Zhang, F.F., Liu, J.J., Wang, J.P., Wang, J.C., 2016b. The genesis of the ores and granitic rocks at the Hongshi Au deposit in Eastern Tianshan, China: constraints from zircon U-Pb geochronology, geochemistry and isotope systematics. Ore Geol. Rev. 74, 122–138.
Wang, Y.H., Zhang, F.F., Liu, J.J., Que, C.Y., 2016c. Carboniferous magmatism and mineralization in the area of the Fuxing Cu deposit, Eastern Tianshan, China: evidence from zircon U-Pb ages, petrogeochemistry, and Sr–Nd–Hf–O isotopic compositions. Gondwana Res. 34, 109–128.
Wang, Y.H., Zhang, F.F., Liu, J.J., Que, C.Y., 2016d. Genesis of the Fuxing porphyry Cu deposit in Eastern Tianshan, China: evidence from fluid inclusions and C-H–O–S–Pb isotope systematics. Ore Geol. Rev. 79, 46–61.
Wang, Y.H., Zhang, F.F., Liu, J.J., 2016e. The genesis of the ores and intrusions at the Yuhai Cu–Mo deposit in eastern Tianshan, NW China: constraints from geology, geochronology, geochemistry, and Hf isotope systematics. Ore Geol. Rev. 77, 312–331.
Wilhem, C., Windley, B.F., Stampfli, G.M., 2012. The Altaids of Central Asia: a tectonic and evolutionary innovative review. Earth Sci. Rev. 113, 303–341.
Williams-Jones, A.E., Migdisov, A.A., Archibald, S.M., Xiao, Z.F., 2002. Vapor-transport of ore metals. Geochem. Soc. Spec. Publ. 7, 279–305.
Windley, B.F., Alexeiev, D., Xiao, W., Kröner, A., Badarch, G., 2007. Tectonic models for accretion of the Central Asian orogenic belt. J. Geol. Soc. 164, 31–47.
Wu, C.Z., Zhang, Z.Z., Zaw, K., Della-Pasque, F., Tang, J.H., Zheng, Y.C., Wang, C.S., San, J.Z., 2006. Geochronology, geochemistry and tectonic significances of the Hongyuntan granitoids in the Qoltag area, eastern Tianshan. Acta Petrol. Sin. 22, 1121–1134 (in Chinese with English abstract).
Xiao, W.J., Zhang, L.C., Qin, K.Z., Sun, S.H.U., Li, J.L., 2004. Paleozoic accretionary and collisional tectonics of the Eastern Tianshan (China): implications for the continental growth of Central Asia. Am. J. Sci. 304, 370–395.
Xiao, W.J., Huang, B.C., Han, C.M., Sun, S., Li, J.L., 2010. A review of the western part of the Altaids: a key to understanding the architecture of accretionary orogens. Gondwana Res. 18, 253–273.
Xiao, W.J., Windley, B.E., Allen, M.B., Han, C.M., 2013. Paleozoic multiple accretionary and collisional tectonics of the Chinese Tianshan orogenic collage. Gondwana Res. 23, 1316–1341.
Xiao, W.J., Han, C.M., Liu, W., Wan, B., Zhang, J.E., Ao, S.J., Zhang, Z.Y., Song, D.F., Tian, Z.H., Luo, J., 2014. How many sutures in the southern Central Asian Orogenic Belt: insights from East Xinjiang-West Gansu (NW China)? Geosci. Front. 5, 525–536.

Xiao, B., Chen, H.Y., Hollings, P., Han, J.S., Wang, Y.F., Yang, J.T., Cai, K.D., 2015. Magmatic evolution of the Tuwu-Yandong porphyry Cu belt, NW China: constraints from geochronology, geochemistry and Sr–Nd–Hf isotopes. Gondwana Res. http://dx.doi.org/10.1016/j.gr.2015.09.003.

Xue, C.J., Chen, B., Jia, Z.Y., Zhang, B., Wan, Y., 2011. Geology, geochemistry and chronology of Lailisigao'er-3571 porphyry Cu-Mo ore-field, western Tianshan, Xinjiang. Earth Sci. Front. 18, 149–165 (in Chinese with English abstract).

Xue, C.J., Chi, G.X., Zhao, X.B., Wu, G.G., Zhao, Z.F., Dong, L.H., 2016. Multiple and prolonged porphyry Cu-Au mineralization and alteration events in the Halasu deposit, Chinese Altai, Xinjiang, northwestern China. Geosci. Front. 7, 799–809.

Yang, F.Q., Yan, S., Qu, W., Zhou, G., Liu, F., Geng, X.X., Liu, G., Wang, X., 2010. The fluid inclusions and C, H and O isotopic geochemistry of the I mineralized zone at the Halasu copper deposit, Xinjiang. Earth Sci. Front. 17, 359–374 (in Chinese with English abstract).

Yang, F.Q., Liu, G.R., Qing, J.H., Zhang, Z.X., Liu, Z.J., Zhang, L.W., Wei, G.Z., Liu, F., Geng, X.X., 2012a. Fluid inclusion and stable isotopes study of Yulekenhalasu copper-(molybdenum) deposit in northern margin of Junggar, Xinjiang. Miner. Dep. 31, 965–982 (in Chinese with English abstract).

Yang, F.Q., Mao, J.W., Pirajno, F., Yan, S.H., Liu, G.R., Zhou, G., Zhang, Z.X., Liu, F., Geng, X.X., Guo, C.L., 2012b. A review of the geological characteristics and geodynamic setting of Late Paleozoic porphyry copper deposits in the Junggar region, Xinjiang Uygur Autonomous Region, Northwest China. J. Asian Earth Sci. 49, 80–98.

Yang, F.Q., Chai, F.M., Zhang, Z.X., Geng, X.X., Li, Q., 2014. Zircon U-Pb geochronology, geochemistry, and Sr–Nd–Hf isotopes of granitoids in the Yulekenhalasu copper ore district, northern Junggar, China: Petrogenesis and tectonic implications. Lithos 190–191, 85–103.

Zang, Y.S., 2014. Geological characteristics and tectonic evolution of Yuhai porphyry copper deposit in Eastern Tianshan Unpublished Master's thesis. Chang'an University, Xi'an, China, p. 62 (in Chinese with English abstract).

Zhai, Y.S., Yao, S.Z., Cai, K.Q., 2011. Mineral Deposits. Geological Publishing House, Beijing (in Chinese).

Zhang, L.C., Xiao, W.J., Qin, K.Z., Zhang, Q., 2006a. The adakite connection of the Tuwu-Yandong copper porphyry belt, eastern Tianshan, NW China: trace element and Sr–Nd–Pb isotope geochemistry. Miner. Deposita 41, 188–200.

Zhang, Z.H., Mao, J.W., Wang, Z.L., Du, A.D., Zuo, G.H., Wang, L.S., Wang, J.W., Qu, W. J., 2006b. Geology and metallogenetic epoch of the Dabate porphyry copper deposit in West Tianshan Mountains, Xinjiang. Geol. Rev. 52, 683–689 (in Chinese with English abstract).

Zhang, D.H., Xu, G.J., Zhang, W.H., Golding, S.D., 2007. High salinity fluid inclusions in the Yinshan polymetallic deposit from the Le–De metallogenic belt in Jiangxi Province, China: their origin and implications for ore genesis. Ore Geol. Rev. 31, 247–260.

Zhang, L.C., Qin, K.Z., Xiao, W.J., 2008. Multiple mineralization events in the eastern Tianshan district, NW China: isotopic geochronology and geological significance. J. Asian Earth Sci. 32, 236–246.

Zhang, Z., Zhou, G., Kusky, T.M., Yan, S., Chen, B., Zhao, L., 2009. Late Paleozoic volcanic record of the Eastern Junggar terrane, Xinjiang, Northwestern China: major and trace element characteristics, Sr–Nd isotopic systematics and implications for tectonic evolution. Gondwana Res. 16, 201–215.

Zhang, Z., Yang, J.T., Zhuang, D.Z., 2010a. Regularity of searching for porphyry copper deposit in Tuwu-Yandong area–the research of prospection model of "three tall and two correspondences and one correlation". Northwest. Geol. 43, 169–183 (in Chinese with English abstract).

Zhang, Z.X., Yang, F.Q., Yan, S.H., Zhang, R., Chai, F.M., Liu, F., Geng, X.X., 2010b. Sources of ore-forming fluids and materials of the Baogutu porphyry copper deposit in Xinjiang: constraints from sulfur-hydrogen-oxygen isotopes geochemistry. Acta Petrol. Sin. 26, 707–716 (in Chinese with English abstract).

Zhang, F.F., Wang, Y.H., Liu, J.J., Wang, J.P., 2015. Zircon U-Pb and molybdenite Re–Os geochronology, Hf isotope analyses, and whole-rock geochemistry of the Donggebi Mo deposit, eastern Tianshan, Northwest China, and their geological significance. Int. Geol. Rev. 57, 446–462.

Zhang, F.F., Wang, Y.H., Liu, J.J., 2016a. Petrogenesis of Late Carboniferous granitoids in the Chihu area of Eastern Tianshan, NW China, and tectonic implications: geochronological, geochemical, and zircon Hf–O isotopic constraints. Int. Geol. Rev. 58, 949–966.

Zhang, F.F., Wang, Y.H., Liu, J.J., Wang, J.P., Zhao, C.B., Song, Z.W., 2016b. Origin of the Wunugetushan porphyry Cu–Mo deposit, Inner Mongolia, NE China: constraints from geology, geochronology, geochemistry, and isotopic compositions. J. Asian Earth Sci. 117, 208–224.

Zhang, F.F., Wang, Y.H., Liu, J.J., 2016c. Fluid inclusions and H-O–S–Pb isotope systematics of the Baishan giant porphyry Mo deposit in Eastern Tianshan, China. Ore Geol. Rev. 78, 409–423.

Zhong, J., Chen, Y.J., Pirajno, F., Chen, J., Li, J., Qi, J.P., Li, N., 2014. Geology, geochronology, fluid inclusion and H-O isotope geochemistry of the Luoboling Porphyry Cu–Mo deposit, Zijinshan ore field, Fujian province, China. Ore Geol. Rev. 57, 61–77.

Zhou, T.F., Yuan, F., Zhang, D.Y., Fan, Y., Liu, S., Peng, M.X., Zhang, J.D., 2010. Geochronology, tectonic setting and mineralization of granitoids in Jueluotage area, Eastern Tianshan, Xinjiang. Acta Petrol. Sin. 26, 478–502 (in Chinese with English abstract).

Zhu, M.T., Wu, G., Xie, H.J., Liu, J., Mei, M., 2012. Geochronology and fluid inclusion studies of the Lailisigaoer and Lamasu porphyry-skarn Cu-Mo deposits in Northwestern Tianshan, China. J. Asian Earth Sci. 49, 116–130.

Zhu, J.J., Hu, R.Z., Richards, J.P., Bi, X.W., Zhong, H., 2015. Genesis and magmatic-hydrothermal evolution of the Yangla skarn Cu deposit, Southwest China. Econ. Geol. 110, 631–652.